Morris, Peter A. (2018) *Quantum ghost imaging.* PhD thesis.

# Quantum Ghost Imaging

Peter A. Morris

A thesis submitted in fulfilment of
the requirements for the degree of
Doctor of Philosophy

School of Physics and Astronomy
College of Science and Engineering
University of Glasgow

December 2018

# Abstract

The process of image recording is arguably one of the most prevalent technology in modern society and continues to inspire vast swathes of research due to its widespread applications spanning military, medical and consumer spheres. The danger present in a field so broad is that separate niches of research can become isolated with critical advancements struggling to traverse the gulfs between. Unifying the field is the omnipresent drive to acquire an ever increasing quality of images at the lowest possible cost, a goal which warrants continual fundamental research.

Quantum entanglement exhibits many intriguing characteristics which make it a suitable tool for such fundamental investigations. The process of spontaneous parametric down-conversion has offered a yet unbeaten strength of photon correlations with the quantum nature of their production providing a reliable and controllable source of single-photons. Arising from these attributes is the technique known as ghost imaging. Though now known to be classically possible, the strength of entanglement generated correlations is yet to be surpassed. This thesis implemented this technique in tandem with the cutting edge detector technology in order to probe the fundamentals of image formation. This form of imaging allowed us to subject an object to a known number of photons whilst acquiring structural information from spatially separate, correlated photons which never interact with the object. The strength of the produced correlations allow us to acquire low background, high resolution images with far less light than traditional techniques and affords many novel benefits. The possibility of incorporating this technique with pre-existent regimes allowed me to draw from advancements made across the landscape of imaging research. Although referred to as "quantum ghost imaging" throughout this work, it should be noted that the intrinsic quantum nature of the correlations was not directly relied upon but provided an ideal source of strongly correlated photons.

In order to determine the limits of a traditional imaging system this thesis first sought to answer the question: "can an image of an object be reconstructed from fewer photons than

pixels in the image?" In chapter 3 I approached this from the perspective of compression, which minimises redundant information within a signal. This lead to the development of an imaging regime capable of imaging with far fewer photons than pixels in the image. By employing assumptions about the sparsity of natural images I was able to reconstruct an image of a biological sample containing an average of less than one photon per image pixel. Having reduced the number of photons necessary to form an image I then considered alternative methods for reducing the optical energy impinging on a sample. I sought to answer the question: "can non-degenerate ghost imaging reduce the optical energy impinged upon an object during imaging". The photons produced in SPDC need not be of similar wavelengths, however may be chosen far from degeneracy, i.e. non-degenerate. In Chapter 4 I presented a ghost imaging system which illuminated the object with infrared light whilst recording the structural information via entangled visible photons. This allowed for objects opaque to visible light to be imaged in high quality without the need for a spatially resolving infrared detector, the state of the art of which lags behind their silicon based visible counterparts. I presented the systems capabilities by imaging objects which were etched into a gold substrate layered on to silicon, both of which are opaque to visible light. Not only did a reduction in energy deposition arise from the lower energy probe wavelength but applying the reconstruction techniques from the previous chapter brought that down to as low as $\approx 16 \; nJcm^{-2}s^{-1}$.

Seeking to expand the repertoire of applications, the low-light capabilities of my ghost imaging were applied to the technique of phase-contrast microscopy in chapter 5. Typically applied to translucent objects, phase-contrast imaging transfers phase information, i.e. the refractive index changed within the object, into an intensity distribution through the use of a phase-filter. In many of these applications the objects tend to be biological in nature, where high optical exposure can result in bleaching or damage. By applying the phase-filter non-locally, i.e. to the photons correlated to those probing the object, I acquired edge-enhanced images of a phase object whilst illuminating with significantly fewer photons than standard phase-contrast techniques.

Having displayed the broad applicability of our low-light ghost imaging system, I then sought to determine the optical resolution in chapter 6. The resolution limits of ghost imaging are not clear at first glance owing to the resolutions dependence upon the strength of spatial correlations. As the length over which the spatial correlations are produced can be brought below the standard diffraction limit, it would seem the resolution of the system could be brought similarly low. To clarify this I artificially restricted the number of spatial modes in each of the correlated beams to uncover the physically realisable resolution. I show that although the resolution of a ghost imaging system to be fundamentally determined by the strength of the correlations, this can never be reached due to the inherent limitations of the intervening imaging system.

# Contents

# List of Figures

# Acknowledgements

First and foremost I owe a debt of gratitude to my supervisor Miles J. Padgett who gave me the opportunity to carry out this research and whose passion and insight inspired me throughout. My thanks also go out to Reuben S. Aspden who taught me the nuances and nuisances of experimental optics and turned the ups and downs into a merry journey. I think myself lucky to have had the support, predominantly in the form of cake and hilarity, of the whole of the Optics group who I believe to be the most enjoyable human beings I could have had the pleasure of working with. Last and most importantly I thank my parents who recognised and stoked my natural curiosity and inclination towards science from a very young age, without their love and support I would not be the man I am today.

# Declaration of Authorship

I hereby declare that this thesis is the result of my own work, except where explicit reference is made to the work of others, and has not been presented in any previous application for a degree at this or any other institution.

Peter A. Morris

# Publications

This thesis is the culmination of the work carried out during my PhD in the Optics group at the University of Glasgow, under the supervision of Prof. Miles Padgett. A list of the peer-reviewed papers co-authored in the three and a half years of the PhD programme is given below.

1 D. S. Tasca, R. S. Aspden, <u>P. A. Morris</u>, G. Anderson, R .W. Boyd and M. J. Padgett, "The influence of non-imaging detector design on heralded ghost-imaging and ghost-diffraction examined using a triggered ICCD camera", *Opt. Express*, 21(30460-73), 2013.

2 <u>P. A. Morris</u>, R. S. Aspden, J. E. C. Bell, R. W. Boyd, and M. J. Padgett, "Imaging with a small number of photons",
*Nat. Commun*, 6(5913), 2015.

3 R. S. Aspden, N. R. Gemmell, <u>P. A. Morris</u>, D. S. Tasca, L. Mertens, M. G. Tanner, R. A. Kirkwood, A. Ruggeri, A. Tosi, R. W. Boyd, G. S. Buller, R. H. Hadfield and M. J. Padgett, "Photon-sparse microscopy: visible light imaging using infrared illumination",
*Optica*, 2(1049-1052), 2015.

4 R. S. Aspden, <u>P. A. Morris</u>, He. Ruiqiung, Q. Chen and M. J. Padgett, "Heralded phase-contrast imaging using an orbital angular momentum phase-filter",
*Journal of Optics*, 18(055204), 2016.

5 P. A. Moreau, E. Toninelli, <u>P. A. Morris</u>, R. S. Aspden, T. Gregory, G. Spalding, R. W. Boyd, and M. J. Padgett, "Resolution limits of quantum ghost imaging",
*Optics Express*, 26(7528–7536), 2018.

# Abbreviations

| | |
|---|---|
| **AWP** | **A**dvanced **W**ave **P**icture |
| **BBO** | $\beta$- **B**arium **B**orate |
| **BS** | **B**eam **S**plitter |
| **CPS** | **C**ounts **P**er **S**econd |
| **DCT** | **D**iscrete **C**osine **T**ransform |
| **DDG** | **D**igital **D**elay **G**enerator |
| **EMCCD** | **E**lectron **M**ultiplying **C**harge-**C**oupled **D**evice |
| **EPR** | **E**instein **P**odolsky **R**osen |
| **FFT** | **F**ast **F**ourier **T**ransform |
| **FOV** | **F**ield **O**f **V**iew |
| **GI** | **G**host **I**maging |
| **HE** | **H**eralding **E**fficiency |
| **ICCD** | **I**ntensified **C**harge-**C**oupled **D**evice |
| **IR** | **I**nfra**R**ed |
| **NA** | **N**umerical **A**perture |
| **PBS** | **P**olarising **B**eam **S**plitter |
| **PPKTP** | **P**eriodically **P**oled **P**otassium **T**itanyl **P**hosphate |
| **PSF** | **P**oint **S**pread **F**unction |
| **QE** | **Q**uantum **E**fficiency |
| **ROI** | **R**egion **O**f **I**nterest |
| **SLM** | **S**patial **L**ight **M**odulator |
| **SPAD** | **S**ingle **P**hoton **A**valanche **D**etector |

**SPDC**      **S**pontaneous **P**arametric **D**own **C**onversion

**TTL**      **T**ransistor **T**ransistor **L**ogic

*"As in nature, all is ebb and tide, all is wave motion."*

Nikola Tesla

# Chapter 1

# Introduction

## 1.1 Preamble

Since the dawn of our species, humanity has sought to capture the essence and beauty of the material world in image. From the neolithic paintings on cave walls to the high definition digital images of today the concept of an image has been entwined with that of art, often designed to evoke an emotional response with the representation of a object. It was not until the efforts of the 19th century French inventor Nicéphore Niépce when he presented the first optically produced image, his "View from the window at Le Gras", that the scientific definition of an image emerged: the optical appearance or counterpart produced from the light of an object. Light was and remains the key. Free from the figurative lens of the human imagination, images became objectively accurate representations acquired directly from the light incident upon an object and so the science of image capturing was born.

Since then, imaging technology evolved hand in hand with the physics of light, research into which pre-dates accurate historical records with evidence of the development of lenses found as early as the ancient Egyptians[1, 2]. Today imaging technologies are advancing at an unprecedented rate with multi-mega pixel cameras now commonplace within first world society, where even the simplest cameras were a novelty in the recent past. With the current prevalence of imaging technologies, one could be forgiven for believing the time of

fundamental research has passed, however a plethora of ground breaking research into the fundamentals of imaging is still under way. The ability to image at extremely low light levels [3, 4], at increasingly higher resolutions [5] and the acquisition of images from light never interacting with the object under investigation [6, 7] are but a few examples of the myriad of technologies arising from such research.

The advent of quantum mechanics brought a paradigm shift in how light was understood, leading to some of the examples above. In this emerging field light was understood as possessing the complimentary qualities of both particle and wave, coming in quantised energy packets as multiples of the fundamental constant $\hbar$, which came to be known as photons. In the ideal lab setting, the concept of a perfect observer so engrained in the scientific method had to be revised and in its place came the concept of the wave function, a reality entwined with its environment, susceptible to change by mere measurements. One curious characteristic arising from the quantum nature of photons is their ability to form entangled states, with a singular wavefunction describing multiple photons. This characteristic is intrinsic to experiments presented here and as such, a comprehensive description of this phenomenon will be provided in the coming paragraph 1.3.

The advancements of detector technology which came hand in hand with an increased clarity of the nature of light, made the reality of individual photons accessible in the lab and brought with it questions concerning the fundamental concepts of image formation. The research undertaken throughout my PhD sought to answer these questions:

"If a typical camera captures in the order of $10^{12}$ photons [8] what is the minimum number of photons required to form an recognisable image?" and "Can the energy impinging upon an object be minimised through the use of less or lower energy photons, whilst capturing images using visible light?"

These questions have significance spanning many imaging applications from covert imaging, where a reduced photon flux leads to higher security, to biological imaging where samples can be degraded with high optical exposures. To answer such questions my colleagues and I adapted our previously developed, ghost imaging system [9] which utilised state of the art

camera technology in conjunction with an entangled photon source to obtain high contrast, essentially background free images. The following body of work shall describe this imaging system in addition to determining the resolution limits of ghost imaging.

This chapter shall present a historical summary of ghost imaging, outlining the theoretical background and highlighting key experimental investigations in recent years.

## 1.2 Ghost imaging

The first demonstration of ghost imaging was given by Pittman *et al.* [10] in 1995 when it was shown that an image could be formed from the coincidence measurements of two spatially correlated yet spatially separated photons. Using spontaneous parametric down conversion (SPDC) the group produced entangled photon pairs for use in imaging. One of the pair probed an object and was detected by a single-pixel detector, whilst the other was recorded using a spatially resolving detector, a scanning fibre. Although neither detector alone was capable of resolving the object, by summing the coincidence measurements from both detectors, a 2D image was formed. The novelty of ghost imaging lies in the fact that all of the spatial information which forms the image comes exclusively from the idler arm such that the image itself is actually formed from photons which never physically interacted with the object, although their correlated partners in the signal arm did. Figure 1.1 shows a simplified schematic of this first demonstration of GI.

The technique was initially presumed to be intrinsically reliant on the quantum nature of the entangled source but there have since been demonstrations of ghost imaging based on purely classical correlations [11, 12]. These systems have typically utilised two classically correlated beams produced from a pseudothermal source [13–17]. In a system such as this, two correlated beams are produced by passing a beam through a spinning ground glass diffuser and dividing with a beam splitter.

The results of systems such as this can be fully predicted using semi-classical photodetection theory. In that treatment the light is treated as a classical electromagnetic field [6] whilst
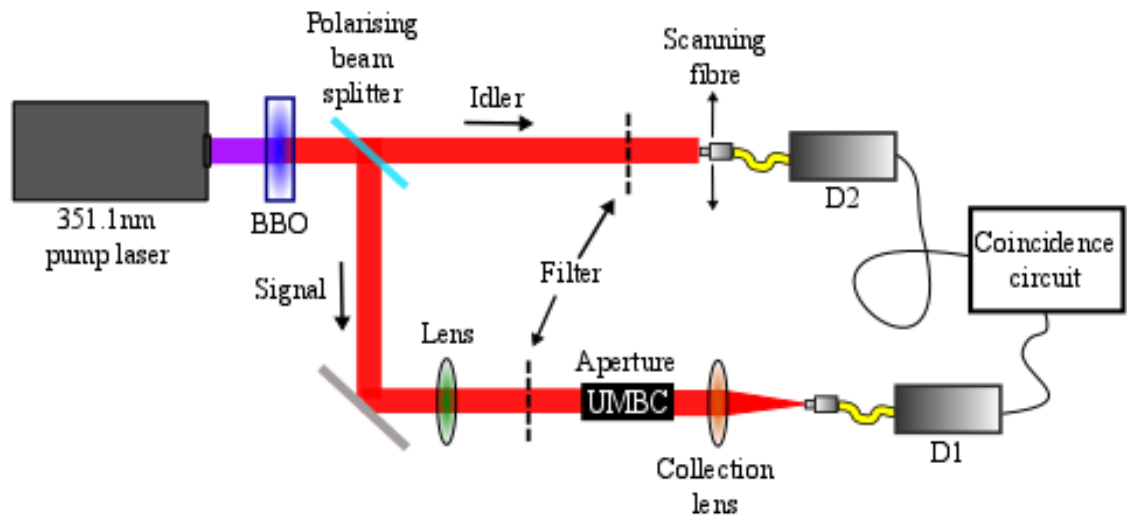
FIGURE 1.1: **Schematic diagram of the first ghost imaging experiment[10].** Correlated photons generated through SPDC were split at a polarising beam splitter. The signal photon is incident on a binary mask containing the initials of their institution (UMBC). Transmitted photons were detected by a bucket detector. The idler photons were detected by raster scanning a single-mode fibre. An image impossible to access via either detector alone was acquired in the coincidence counts.

the charge carriers in the detector which the light excites are considered quantised. Further analysis has shown that classical set-ups can almost fully replicate the results of their quantum counterparts bar the ability of quantum ghost imaging to obtain high contrast images in multiple planes using a fixed source [12]. It is the strength of these correlations which is unique to their quantum nature and this disparity has allowed for tests of quantum mechanics to be developed such as the Bell inequality[21].

Prior to the system presented here, all previous examples of quantum ghost imaging relied upon the use of a scanning fibre as the spatially resolving detector. This fundamentally limited the detection efficiency. However, the system first developed by Aspden *et al.* [9] has overcome this limitation by the use of an intensified CCD (ICCD) as the spatially resolving detector. This allowed for the capture of images over the full field of view (FOV) rendering the system practical for developing an imaging system capable of capturing high quality images with very few photons.

## 1.3    Correlations and quantum entanglement

The experiments presented throughout this thesis were facilitated by spatial correlations present between entangled photons. Entanglement is defined as a quantum state which cannot be described separately from one or more other states in which properties such as postion, momentum etc. are strongly correlated. In a brief mathematical description following that presented in reference [19], we represent a pure quantum state of two quantum systems, a and b as a two-state quantum mechanical system,

$$|\psi\rangle = |\lambda\rangle_a|\phi\rangle_b. \tag{1.1}$$

It is stated in the superposition principle that any product of these two states of the system is also an allowed state of the quantum system and we can represent this as,

$$|\psi\rangle = \frac{1}{\sqrt{2}}(|0\rangle_a|0\rangle_b + |1\rangle_a|1\rangle_b). \tag{1.2}$$

It is impossible to express this superposition of product states as a product of one state for system a and a separate state for system b as in equation 1.1. Being in a superposition of states alone does not guarantee entanglement, however the impossibility of expressing the state as product of pure states defines the state as entangled. One can see from equation 1.2 that a measurement on one part of the state provides information about the other, regardless of its locality. It is this counter-intuitive result which leads to Einstein's famous expression "spooky action at a distance". It was not the apparent superluminal information transfer which shed doubt but that these quantum correlations were simultaneously present in complimentary bases. In their seminal paper [20] Einstein, Podolsky and Rosen argued that the ability to infer the position of a particle and its momentum from a measurement made to another non-local particle was a violation of the Heisenberg uncertainty principle. This misunderstanding will be discussed in chapter 6. One could talk at length about the

progress of research concerning quantum entanglement and the work undertaken to measure its strength [22–25], however this would go beyond the scope of the research presented here.

There are many available sources of correlated photons both classical and quantum. The latter has been opted for in the experiments presented here both for their strength in complementary bases and more importantly the extremely short timing resolution of their production. The process chosen to generate our entangled photons was spontaneous parametric down-conversion. The details of the process and its possible sources shall be outlined in the following section.

## 1.4 Spontaneous parametric down-conversion

An abundance of research has been carried out on the nature of the correlations produced by SPDC [26–30] which was first discovered in 1970 by Burnham and Weinberg [31]. It is a non-linear process governed by the second order non-linear susceptibility ($\chi^{(2)}$) [30, 32] within a crystalline medium. This susceptibility arises due to the induced dipole moment per unit volume ($P$) within the crystal, described as[33]:

$$P = \epsilon_0[\chi^{(1)}E + \chi^{(2)}E^2 + \chi^{(3)}E^3 + ...],\tag{1.3}$$

where $E$ is the amplitude of the electric field. A high energy pump photon interacts with the crystal producing two lower energy photons termed the signal and idler. Like all physical processes the resultant photons obey the conservation of energy and momentum laws which result in what are called the phase-matching conditions [31]:

$$\boldsymbol{k}_p = \boldsymbol{k}_1 + \boldsymbol{k}_2,\tag{1.4}$$

$$\omega_p = \omega_1 + \omega_2,\tag{1.5}$$

**a) Collinear phase-matched**

$k_i$ $k_s$

$k_p$

**b)  Non-collinear phase-matched**

$k_i$ $k_s$

$k_p$

**c) Collinear phase-mismatched**

$k_i$ $k_s$ $\Delta k_z$

$k_p$

**d) Non-collinear phase-mismatched**
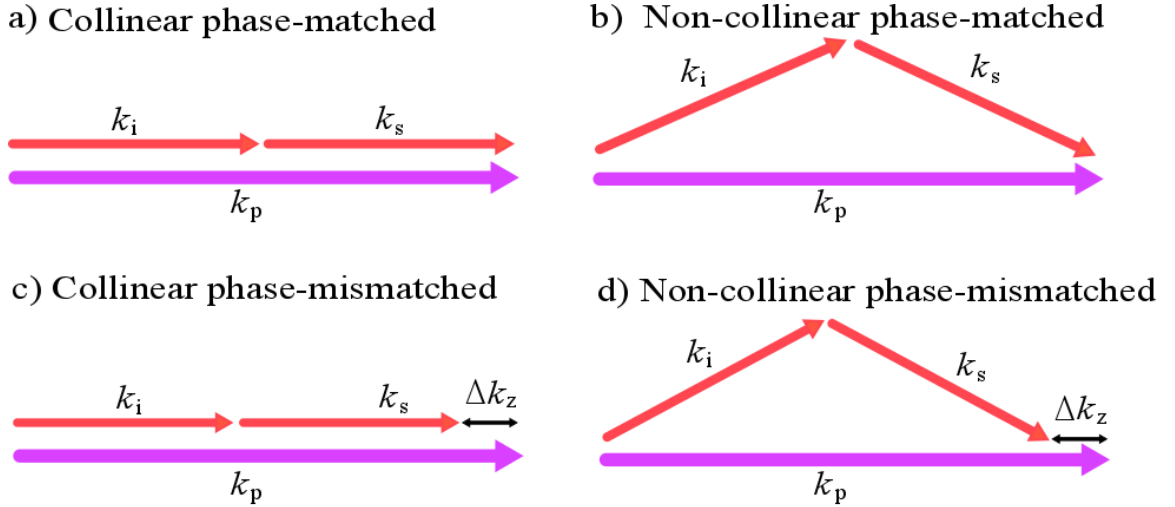
$k_i$ $k_s$

$\Delta k_z$

$k_p$

FIGURE 1.2: **Phase-matching conditions of SPDC:**a) Phase-matched collinear b) Phase-matched non-collinear c) Phase-mismatched collinear d)Phase-mismatched. Note the phase-mismatch $\mathbf{\Delta k}_Z$ is only in the longitudinal direction, transverse momentum is conserved.

where $\mathbf{k}_{(p,1,2)}$ and $\omega_{(p,1,2)}$ are the wavevectors and frequencies of the pump, signal and idler photons respectively. In the majority of experiments presented here the energy of the output photons is split equally giving degenerate signal and idler, each half the energy of the pump photon. However, they can also be produced far from degeneracy affording the opportunity to carry out very interesting research such as that presented in chapter 4 and in references [34–36].

There is a permissible mismatch, $\mathbf{\Delta k}_Z$, between the wavevectors of pump which the conversion efficiency depends upon, scaling with $\mathrm{sinc}^2 \frac{\mathbf{\Delta k}_Z L_z}{2}$. Peak efficiency is achieved when perfectly phase-matched i.e. $\mathbf{\Delta k}_Z = 0$. Shown in figure 1.2, the signal and idler beams can be produced collinear or non-collinear to the optical axis of the pump beam.

The phase-matching of the SPDC can be tuned via altering the refractive index the photons experience within the crystal, made possible by the refractive index's dependence on the frequency of light. How the refractive index is changed depends on the type of crystal in use but is most commonly achieved by utilising the birefringence of the material. When this is not possible, i.e. the crystal is not birefringent, this is achieved by periodically inverting the

axis of the crystal to achieve quasi-phase-matching[33]. The two most commonly used non-linear crystal material are $\beta$-barium borate (BBO) and periodically poled potassium titanyl phosphate (PPKTP). PPKTP is an example of a birefringent crystal and can only achieve quasi-phase-matching, however it can achieve a magnitude greater brightness than BBO reaching up to $\approx 3x10^5$ pairs per second [37]. Several characteristics of the experiments presented here were better suited to a BBO source rather than PPKTP. For one, we sought to operate our systems at extremely low-light levels with the ability to count detected photons and secondly, our imaging system employed extremely short detection windows to eliminate background noise 2.2. Both of these technqiues would difficult to achieve with PPKTP given its brightness in comparison to the low production rate of BBO. This also proved advantageous as the phase-matching of BBO is temperature independent unlike PPKTP [38, 39] giving one less restriction on the experimental environment. The phase-matching of the BBO could be tuned simply by rotating the crystal axis in respect to the input pump beam.

As seen in figure 1.3 SPDC comes in two forms characterised by the relationship between signal, idler and pump polarisation states. If both signal and idler are similar polarisation to the pump it is known as type-I. Conversely if the signal and idler are differently polarised it is known as type-II. Type-I SPDC was used throughout this thesis as the spatial correlations are easier to utilise, there being no offset between signal and idler cones and no polarisation difference between the beams to take into consideration.

In summary, the experiments throughout this thesis all utilise type-I SPDC produced in BBO crystals as a source of correlated photon pairs. The desire for low light levels, the ease of phase-match tuning and the temperature independence make them an ideal source of correlated photons.

## 1.5 Theoretical background

I shall now provide a basic theoretical foundation to ghost imaging, describing the probability of obtaining an image of the object in coincidence measurements. I will begin with an
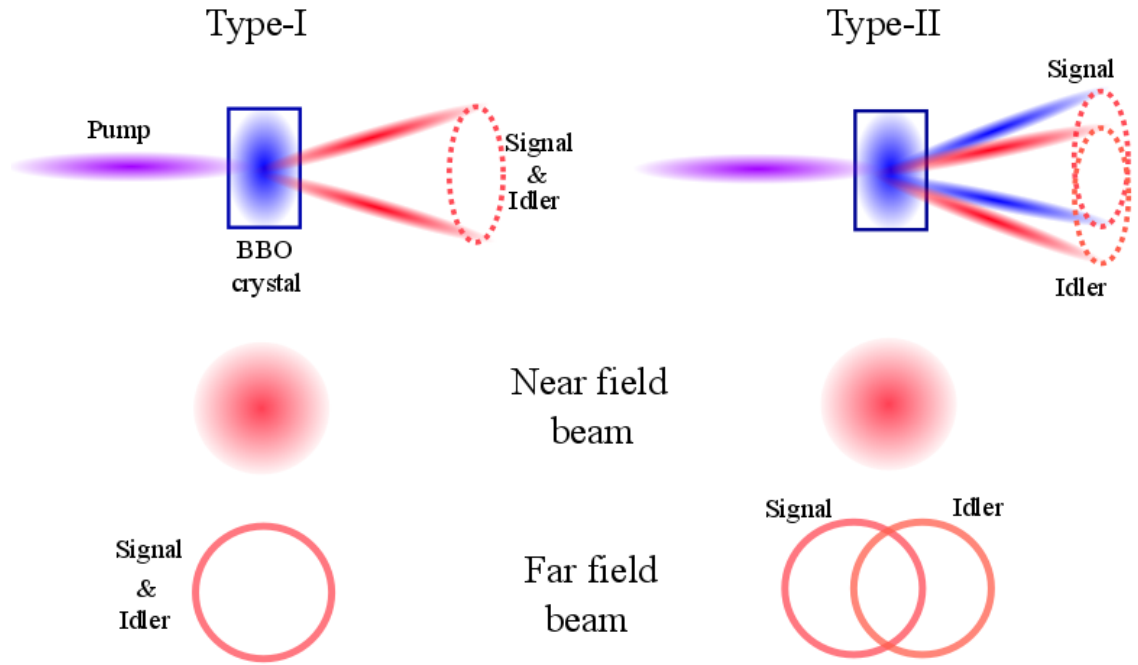
FIGURE 1.3: **Spontaneous parametric down conversion.** Type-I and type-II SPDC and the transverse beam profiles in the image plane and far-field of the source. The ring diameters in the far-field vary with the phase-matching conditions.

explanation of the aforementioned Pittman experiment where the heralding detector is a scanning fibre before drawing a comparison with our full field of view system, highlighting the benefits of using a multi-pixel detector. We begin by assuming our down-converted photons are produced degenerately through the SPDC process using a pump beam with a large Gaussian transverse profile. With these assumptions in mind we can describe our entangled two-photon field as:

$$|\Psi\rangle = \int d\eta_S d\eta_I \Psi(\eta_S, \eta_I) |\eta_S\rangle |\eta_I\rangle, \tag{1.6}$$

where $\eta_{S,I}$ represent the transverse coordinates of signal and idler photon at the source and $|\eta\rangle$ is the pure state of a single photon in transverse position $\eta$ [30, 40, 41]. Assuming an Einstein, Podolsky, Rosen (EPR) like non-separable state [20] we can write the transverse wavefunction $\Psi$ as:

$$\Psi(\eta_S, \eta_I) = T(\eta_S + \eta_I)\Gamma(\eta_S - \eta_I), \tag{1.7}$$

where we take T as the transverse pump profile of the beam and $\Gamma$ as the Fourier transform of the phase-matching function. As has been previously shown [9, 30, 40] since $\Gamma$ is much narrower than T, the transverse positions of the photons are correlated. The paths of signal and idler are then separated with signal propagating to the single-pixel detector via the object and idler propagating to the spatially resolving detector. If we take the transmission function of the object to be A, where $A = A^*$ (i.e. the function is real), we define $g_S(\eta_S)$ as the transfer function of the spatial properties of the beam from crystal to detector. This function is a convolution of the relay optics and aperture function. Assuming the single-pixel detector detects across all spatial modes, the detection of a photon is described by:

$$|\phi_S\rangle = \int d\eta_S g_S(\eta_S) |\eta_S\rangle, \tag{1.8}$$

The idler propagates through the system and is measured using a scanning single mode fibre detector and its spatial state is described as:

$$\left|\phi_I^i\right\rangle = \int d\eta_S f_i(\eta_S) |\eta_S\rangle, \tag{1.9}$$

where $f_i(\eta_S)$ is a function of the spatial properties of the beam at each detection point, i, of the scanning fibre and over the full field of view $\sum_i^N f_i(\eta_S) = g_S(\eta)$, where N is the number of detection points.

We can now represent the probability of a coincidence detection at each detection point of the scanning fibre as:

$$P_i = |\langle\phi_1|\langle\phi_2^i|\Psi_{1,2}\rangle|^2 = \int\int d\eta_1 d\eta_2 \Psi(\eta_1, \eta_2) A^*(\eta_1) g^*(\eta_2) f_i^*(\eta_2). \tag{1.10}$$

From equations 1.8 and 1.9 we see that no image of the object is obtainable from either detector as there is no spatial resolution at the single pixel detector and no object information at the scanning fibre. Equation 1.10, however shows a clear dependence on both the aperture function of the object and upon the spatial information from the scanning fibre. In order to obtain an image from the coincidence measurements at each detection point, we define the average number of detected photons at point i to be:

$$\langle M_i \rangle = M Q_i P_i, \tag{1.11}$$

where $Q_i$ is the probability of detection at each $i^{th}$ point, 1/N in the case of scanning fibre and M is the number of generated photon pairs. Summing over many coincidence measurements, across the full field of view, an image of the object is obtained:

$$G(\eta) = \sum_i^N \langle M_i \rangle \delta(\eta - \eta_1). \tag{1.12}$$

As discussed above, this detection probability is fundamentally limited by its dependence on the scanning fibre scanning N detection points, greatly increasing the number of photons necessary to form an image. In the experiments to follow we utilise a full FOV camera in place of this scanning fibre allowing us to measure across all detection points simultaneously, increasing our detection efficiency by a factor of N. Each measurement is now multi-dimensional, asking "which pixel are you in" as opposed to the previous "are you in this pixel?" removing the dependence on $Q_i$. By use of a time delay between detector measurements, which will be elaborated on in following sections, each measurement can still be described as a coincidence measurement. In this regime the average number of detected photons in each $i^{th}$ pixel of the image is:

$$\langle M_i \rangle = M P_i, \tag{1.13}$$

whilst the probability of detection is unchanged, we have removed the dependency on the detectors position, hence increasing the detection efficiency by a factor of N. From equation (1.14) we see our imaging system is clearly only reliant on the number of coincidence measurements made and not the number of pixels sampled.

## 1.6 Walkthrough

Now that the historical and theoretical foundation of quantum ghost imaging has been presented, the following chapters shall provide a rigorous investigation into ghost imaging, its benefits over classical imaging techniques and several novel approaches to imaging not possible with traditional techniques. As each of the experiments performed throughout this body of work utilise similar techniques and apparatus, the following chapter will provide a comprehensive summary of those factors and the process of their construction and alignment. The remaining chapters will then present a series of ghost imaging experiments and how their results reflect upon the technique and its possible applications. The findings of this body of work will then be summarised, linking the advancements made in each individual experiment, followed by a discussion concerning the future of the field.

# Chapter 2

# Experimental methods

## 2.1 Introduction

Each experiment presented throughout this thesis is a variation of a general ghost imaging system and is based on similar experimental set up and methodology. This chapter will give an overview of the system whilst postponing an in-depth description of individual experiments to their respective chapters. Figure 2.1 shows a schematic of the ghost imaging system displaying the major components similar to each experiment.

As mentioned above, the system relies upon the spatial correlations between photon pairs produced by the SPDC process. The source of correlated photons is a 355 nm laser pumping a $\beta$-barium borate (BBO) crystal. Due to the phase-matching conditions discussed previously, the signal- and idler-photons display strong (anti-) correlations in their (momentum) position. The correlated photons are separated at a probabilistic beam splitter into the signal (a) and idler (b) arms of the system. The possible paths the photons take at the beam splitter is represented by a superposition of states:

$$|2\rangle_a|0\rangle_b + 2|1\rangle_a|1\rangle_b + |0\rangle_a|2\rangle_b. \tag{2.1}$$

In ghost imaging the state where a photon has been transmitted into each arm of the experiment i.e. $|1\rangle_a|1\rangle_b$ is measured and we refer to the photon in the SPAD arm as the signal photon and that in the camera arm as the idler photon. In this case the signal photon is incident upon the object under investigation, typically a partially transmissive real object or a partially reflective object displayed on a liquid-crystal spatial light modulator (SLM). The object is placed in either the near- or far-field of the crystal to access the strongest spatial correlations. The transmitted (reflected) photons are gathered by a collection lens and detected by a heralding-detector: a fibre coupled single-photon avalanche detector. The photo-detection signal from said detector is used to herald the arrival of the idler photon at the second detector, in this case a camera. The idler photon propagates through a image-preserving optical delay line used to account for lag of the electronic trigger signal between the two detectors.

The idler photon is incident upon the full field-of-view (FOV), spatially resolving detector placed in the image plane (ghost imaging) or far-field (ghost diffraction) of the object. The detector used is an intensified charge coupled device (ICCD) and is triggered such that it records only those photons correlated to the signal photons detected by the heralding detector. The details of this trigger mechanism are discussed in the next section.

The effects of other two states of the system $(|2\rangle_a|0\rangle_b + |0\rangle_a|2\rangle_b)$, where both photons enter the same arm of the experiment, are considered negligible. When both photons enter the detector arm the ICCD is triggered but captures no correlated photons and when both enter the camera arm they go undetected as the ICCD is not triggered.

## 2.2 Experimental apparatus

### 2.2.1 Source characteristics

The sources of correlated photons used were a range of BBO crystals pumped by a pulsed ultraviolet laser. The pump source was a JDSU Xcyte laser producing 355 nm photons of 10 ps pulse duration at a repetition rate of 100±10 MHz. The UV photons were generated
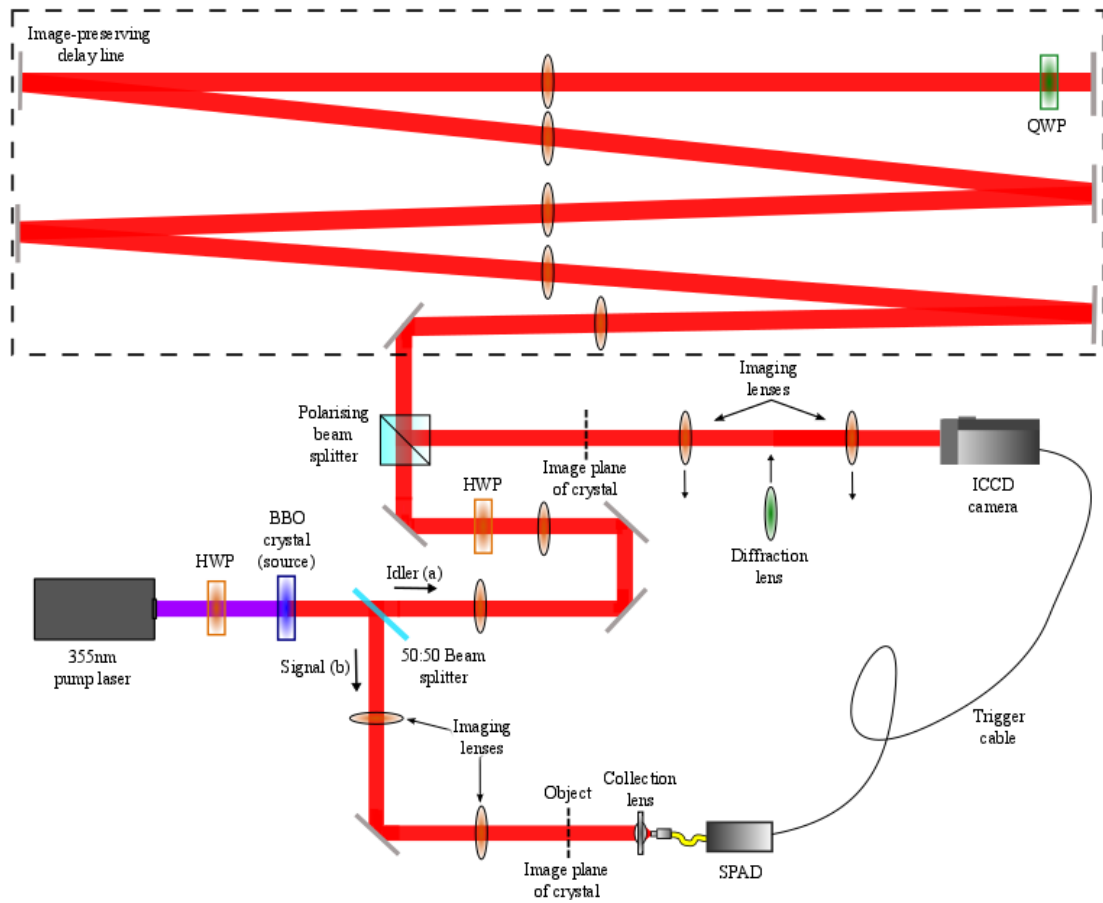
FIGURE 2.1: **Simplified experimental set-up:** Down-converted entangled photon pairs are generated collinearly by pumping a BBO crystal with a 355 nm laser. Both the object and ICCD camera are placed in either imaging or far-field planes of the crystal where the down-converted photons exhibit the strongest spatial correlations.
Photon-pairs are split at a beam splitter resulting in one probing the object before being detected by a single-pixel SPAD whilst the other is re-imaged to a spatially resolving ICCD camera. The camera was triggered by the signal representing a detection from the heralding detector. The intrinsic electronic delay was accounted for by use of an image-preserving delay line to ensure the camera and heralding detector were detecting correlated photon pairs as opposed to spurious, uncorrelated photons.

by a frequency tripled Nd:YAG laser and as such it was necessary filter out spurious laser lines. In several experiments the beam was focussed on to a high-precision pinhole 50 $\mu$m to spatially filter the beam, the Airy spot from this was recollimated to approximate a Gaussian at the input facet of the crystal. The BBO crystals were mounted in Thorlabs Polaris mounts to provide optomechanic tilting in the horizontal and vertical axis, which allowed the tuning of the phase-matching conditions. The production rate of down-converted

photons produced in the crystal was tunable through the implementation of neutral density filters and/or a half-waveplate, as BBO crystals exhibit polarisation-dependence. Due to the nature of the coincidence measurements and photon counting scheme employed, the pump beam was often attenuated to ensure ≪1 photon-pairs were produced per pulse of the UV-pump laser. The correlated photon pairs were then selected with an interference bandpass filter with a 10 nm wide transmission window centred on 710 nm, thereby removing spurious photons such as residual pump, stray and fluorescence photons.

### 2.2.2 Heralding detectors

The heralding detector in each of the following experiments did not record any spatial information of the incident photons but provided a purely binary measurement of their presence. This produced a transistor-transistor logic (TTL) pulse which was used to trigger the intensifier of the ICCD camera. The signal beam was focused by a collection lens to the input facet of a fibre coupled to the SPAD. In ghost imaging a multi-mode fibre is typically used to couple as many spatial modes as possible in order to maximise the efficiency and FOV of the system.[41] Where mode selectivity was necessary, such as in ghost diffraction (6) or phase imaging (5), the detector was coupled to a single-mode fibre. The effects of mode selectivity on specific ghost measurements will be discussed in their relative chapters.

The majority of the experiments which will be discussed in later chapters used correlated degenerate SPDC, where both signal and idler were produced at 710 nm. In those experiments a SPCM-AQR series single-photon avalanche detector (SPAD) produced by Perkin Elmer was used to detect the photons entering the signal arm. This had a silicon based active detection area of 175 $\mu m^2$ and a quantum efficiency (QE) of ≈70 % at 710 nm. The number of thermalised photo-electrons (dark counts) produced was of the order ≈1000 counts per second (CPS). This detector produced the 15 ns long TTL pulse used to trigger the ICCD camera.

In the experiment presented in chapter 4, where the signal photons generated were at 1550 nm, the aforementioned detector had to be substituted for one sensitive to such

infrared (IR) wavelengths. This SPAD was based upon InGaAs/InP (Indium Gallium Arsenide/Indium Phosphate) and was designed to detect telecoms bandwidth photons. It was cooled to ≈-40 °C using an inbuilt Peltier device, had a QE of ≈25% and dark count rate of ≈9000 CPS at 1555 nm. It was free-space coupled with an active square detection area of 625 $\mu m^2$ with a numerical aperture NA of 0.7. This NA and the magnification of the relay optics resulted in a coupling efficiency of ≈50%. There was a small probability that the SPAD would trigger from the previous photo-detection in an effect known as after-pulsing. This was combated by setting a hold-off time after each detection in which the detector was unresponsive to incoming light, however, this inherently limited the trigger rate. The hold-off time was set to 10 $\mu s$, limiting the maximum count rate to 100 kHz. To further reduce the rate of false detections the detector was synchronised to the pulsing of the pump, operating the SPAD in time-gated mode rather than free-running. This allowed for us to set an short gate width of 1.4 ns, further negating the detection of stray photons in the system.

### 2.2.3 Spatially resolving detectors

The images acquired in each of the following experiments were captured using an Andor IStar intensified CCD camera (ICCD). An ICCD operates by converting incoming photons into photoelectrons, in its intensifier tube. These electrons fluoresce on a phosphor screen to produce photons which are subsequently detected by the CCD chip [42]. This chip composed of 1024×1024 pixels, each 13.3 $mm^2$ and was cooled to -30°C. The resolution of the camera was set by the photo-multiplication process. This manifested itself as photo-events spilling across several pixels on the chip, in a process known as blooming. This effect factors into our photon-counting procedure which is outlined in section 2.5.1. The typical size of the idler beam allowed for a smaller region of interest (ROI) to be specified on the chip, which allowed faster read-out times and smaller data files. An ICCD was chosen over other imaging technologies, such as electron multiplied CCDs (EMCCDS), for its ability to utilise extremely narrow timing resolutions [42, 43]. There are two timings of pertinence; the exposure time and the gate width. The exposure time is the length of time which the

signal is accumulated on the CCD chip before it is read out, typically set to <2 s. The gate width is the length of time the intensifier fires during each exposure and in our experiments was of the order of nanoseconds, firing multiple times per exposure. The intensifier can be triggered by an internal or external signal. Internal triggering mode sets the trigger time from the cameras own digital delay generator (DDG), allowing the delay and width of the intensifier to be manually controlled. External trigger mode utilises a signal, such as the TTL pulse from the heralding detector, to trigger the intensifier. When external triggering the intensifier gate width can be set to either direct gate mode, where the intensifier fires for the length of the incoming TTL pulse or can be set manually with the DDG.

### 2.2.4 Trigger mechanism

As mentioned previously, our source of correlated photons was attenuated such that on average ≪1 photon pair was produced per pulse of the pump laser, corresponding to every ≈10 ns. This allowed for the width of the intensifier gate width to be set such that the intensifier was only active for several nanoseconds during which a photon was expected to arrive. This essentially negated any background light in the system. In order to access the spatial correlations of our photon pairs, the triggering of the intensifier had to be synchronised to the correct pulse of the laser source. The idler photon had to arrive during the time the intensifier was triggered by the detection signal of its correlated twin at the heralding detector. To account for the electronic lag between a signal photon detection and the firing of the intensifier the idler photon propagated through over ≈20 meters of image preserving delay line (the exact length of which varied between each experiment) as shown in 2.1, whilst fine timing adjustments were controlled by the camera DDG. This delay line was composed of a series of 1 m focal length telescopes through which the beam propagated twice. The beam was coupled into the delay line using a half wave plate (HWP) and polarising beam splitter. Within the delay line the beam double passed a quarter wave plate (QWP), thus rotating the polarisation, such that the polarising beam splitter reflects the beam towards the ICCD on its return path.

## 2.3 Klyshko advanced wave picture

Thus far it has been shown that the strong spatial correlations exhibited by SPDC produced twin photons could be utilised in a novel imaging technique. Despite the quantum nature of these correlations, Klyshko [44] presented an argument based purely on classical geometric optics, which could fully replicate the spatial distribution of a ghost imaging system (1.5). His Advanced Wave Picture (AWP) replaced the heralding detector with a light source which then propagated back through the intervening optics to the plane of the crystal. In essence we can view those back propagating photons as a time-reversal of the signal arm of our ghost imaging system, with each signal and idler pair replaced by a singular photon. Here the crystal assumed the role of a mirror, reflecting the back propagating beam into the idler arm of the system to the ICCD camera. The resultant intensity distribution recorded at the detector, be it in the far-field or image plane of the crystal, matched that achieved by the system when operated in the ghost imaging regime. The only discrepancies arose where the crystal was tilted or a divergent/convergent pump beam was used. In those cases the crystal was replaced by a tilted or curved mirror to directly match the ghost imaging results. Figure 2.2 shows a comparison of unfolded schematics of our ghost imaging with that of the AWP in an imaging configuration. All aspects of the heralding detector (numerical aperture, mode composition etc.) map directly on to the characteristics of the source in the AWP.

## 2.4 Alignment

The AWP not only functioned as a predictive tool but also as an accessible test bed for new experiments and as an invaluable alignment tool. When aligning over 20 meters of optics there were several criteria that had to be met in order to repeatedly acquire high fidelity images. The numerical aperture and field of view of the heralding detector had to overlap with that of the down-converted field with both signal and idler beams propagating through the centre of all the intervening optics. By replacing our heralding detector with a
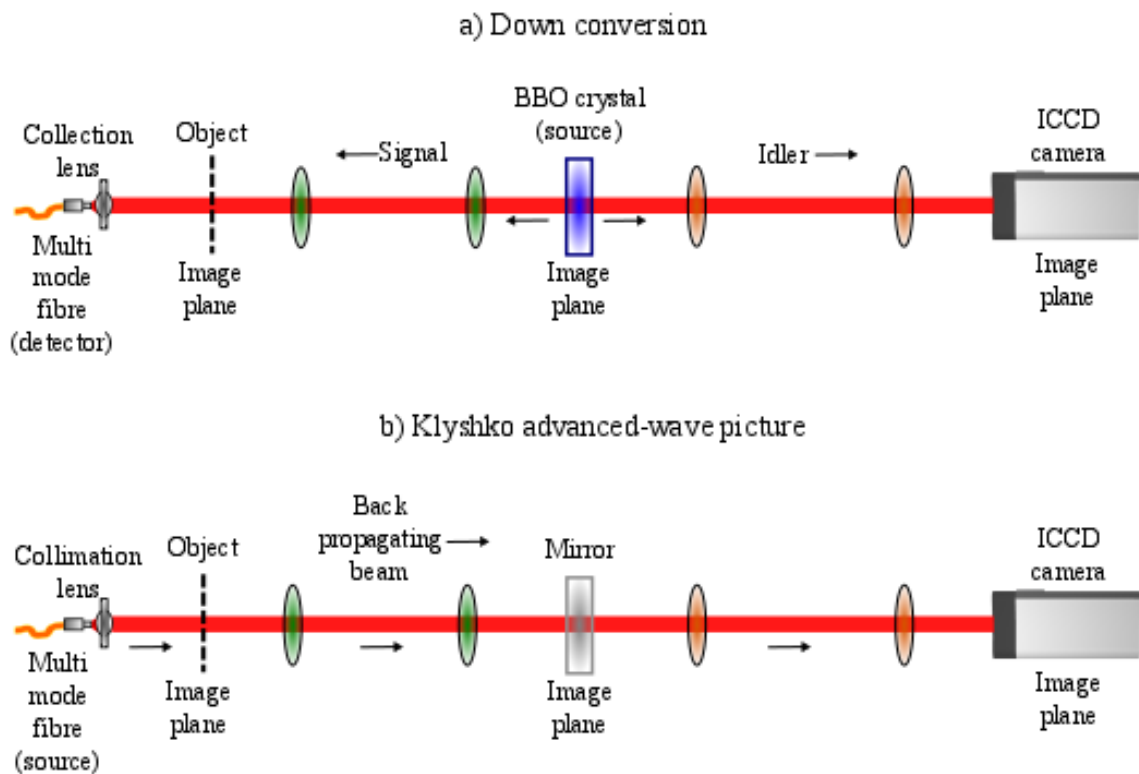
FIGURE 2.2: **(a) Unwrapped simplified schematic of the ghost imaging system:**
After the BBO crystal the signal and idler take spatially separate paths. The signal
interacted with the object, placed in an image plane of the crystal whilst the idler
propagates to an ICCD also placed in an image plane. **(b) Unwrapped Klyshko
Advanced Wave Picture:** In this representation the heralding detector is replaced by
a classical source which propagates backwards through the signal arm. The BBO crystal
acts as a mirror, reflecting photons into the idler arm and onwards to the camera. This
could accurately replicate the spatial distribution acquired in a ghost imaging regime
with only slight disparity if a divergent/convergent pump beam was used.

visible laser diode and back-propagating this beam, it overlapped perfectly with the down-
converted light in the image planes of the crystal. Being of sufficient brightness to see with
the unaided eye the beam was then used to align the system. The slight displacement of
the back-propagated beam in the momentum planes of the crystal, due to its tilt, gave rise
to difficulties when aligning the far-field but was remedied with the following procedure.

All of the experiments presented in the following chapters were initially constructed and
aligned following the same procedure, which will now be outlined. Initially the input mode
to the crystal was set by focusing the laser output through a pinhole before recollimating
to the crystal. This beam was initially aligned through a set of pinholes in the image plane

and far field of the crystal. A low power diode laser at 710 nm was reflected into the path by a removable mirror to provide a visible beam which was aligned through the pinhole set. This beam was then aligned to both detectors through the center all of the optics. Its position in the near and far field were overlapped onto the ICCD and the position recorded. The fibre which couples to the heralding detector was set in a 6-axis mount allowing for the fine control of its position and angle. The coupling efficiency of the alignment beam was initially optimised by observing the output off the fibre. Once this was aligned to both detectors, the down-converted light was passed through the system and the idler beams position checked on the ICCD. Any discrepancies in the near and far-field were then adjusted for. The coupling of signal beam to the detector was then optimised via the 6-axis controls of the fibre mount with the fibre connected to the heralding detector and the counts were maximised. In order to align the object under examination the AWP was again used. If the previous stages of alignment were carried out thoroughly, the back propagated beam overlapped with the down converted beam in the image plane of the camera. The object, either on a 3-axis controlled mount or displayed upon a SLM, was then placed in the system and aligned in real time until a clear image was acquired by the ICCD. At this stage the system was preliminarily tested in a ghost imaging regime and if required, final adjustments made to alignment before data acquisition.

## 2.5 Data analysis

### 2.5.1 Photon counting

The images acquired in each of the following experiments were composed of multiple exposures from an ICCD camera, each triggered by the detection of signal photons by the heralding detector. Through the attenuation of the source it was ensured that on average $\ll 1$ photon pair was produced per pulse of the laser i.e. per exposure [41]. The length of the exposures was chosen to maximise the heralding efficiency (HE) of the system. This is defined as the percentage of idler photons detected per signal photon detection and is

the typical measurement of efficiency used to characterise ghost imaging systems. The optimum exposure time was found to be typically $\leqslant 2$ s, varying slightly with the generation of the camera used and as our understanding of the system solidified.

To determine the HE of the system a photon-counting methodology for the final images was composed [9]. This process was carried out for individual frames before their subsequent summing into the final images. When a photon is detected at a pixel the charge tends to bleed into neighbouring pixels in an affect called blooming. To capitalize on this we attributed any events smaller than two pixels to read-out noise on the chip and subtracted them from the frame. The noise probability per pixel was then calculated by acquiring 100 triggered frames with the shutter closed. This was plotted as a histogram allowing a threshold based upon the dark-count probability per pixel to be set. Any signal above the threshold was determined to be a photon whilst removing anything falling below. This allowed for the binarisation of each frame which were summed to give the final images containing a known number of photons. As the binarisation was set by the threshold, it could not determine between one or many photons, thus to accurately count the detected photons it was necessary to capture no more than one photon per exposure. The ICCD software had its own internal cosmic ray correction.

### 2.5.2 Contrast

The most commonly used figure of merit for defining image quality used throughout this body of work was the contrast of the acquired images. The contrast of our acquired images was a function of the optical efficiencies in both signal and idler arms of the system, in addition to the characteristics of the source and of both detectors. Each of the heralding detectors had an inherent dark count rate which did not appear in the final images but triggered the ICCD at random intervals. Each false triggering of the camera brought the possibility of detecting photons from the crystal which were not correlated with any image information. The effect of this was to create a background level mapped to the emission of the source, limiting the contrast of our images. The contrast of our final data was defined as:

$$Contrast = \frac{I_{max} - I_{min}}{I_{max} + I_{min}}.$$

(2.2)

# Chapter 3

# Compressive ghost imaging

## 3.1 Introduction

The ghost imaging systems presented in this chapter allowed for the acquisition of images with negligible background in addition to the ability to accurately count the number of photons present in each image. With this system operational I sought to answer the question: "Can an image of an object be reconstructed from fewer photons than pixels in the image?" As the subtleties of what constitutes "an image" was beyond the scope of this work, I adhered to the basic definition provided in section 1.1: the optical appearance produced from the light of an object. Currently, the images recorded with conventional cameras typically contain $10^{12}$ photons [8]. Since the Poissonian noise associated with the detection of individual photons scales with the square root photon number, i.e. $10^6$ photons, it is drastically outweighed by other noise sources [45]. The ability to image using far fewer photons would have numerous applications spanning many diverse fields of interest. For example; in biological imaging a high flux can cause sample damage or

---

This chapter contains material published in the following paper:

bleaching and in covert applications a reduced flux offers increased security. Three distinct experimental configurations based on coincidence measurements were investigated for use in low-light imaging. The configuration which gave the highest quality low-light images was then determined and used to acquire under-sampled date, i.e. images containing fewer photons than were necessary to resolve the object. These images were then passed through our compressive sensing inspired reconstruction algorithm. The algorithm relied upon the natural sparsity of spatial frequencies which the majority of natural images exhibit, the same characteristic which allows for low loss image compression. The combination of our low-light imaging system and reconstruction algorithm enabled the acquisition of images of a biological sample, containing fewer photons than there were pixels within the image.

This chapter will first discuss the specific details of the experimental set up and how it was characterised in the three different configurations for low-light image acquisition. I shall then introduce the theoretical foundation of the reconstruction technique which allowed us to acquire images containing an extremely low number of photons. The process of optimising the reconstruction will be discussed before analysing the final images. The findings will then be summarised and the results discussed with respect to comparable techniques.

### 3.1.1   Contributions

The work reported in this chapter was carried out in collaboration with three other group members and with the input from Robert Boyd of the University of Ottawa. The concept of applying compression inspired reconstructed algorithms to our ghost imaging data arose during discussions between Miles J. Padgett and Robert W. Boyd. The original experimental system was constructed by Reuben S. Aspden and was further developed by myself for low-light biological imaging. The results taken were acquired by myself and the reconstruction algorithm was designed by both M. J. Padgett and myself with help from Jessica E. C. Bell whilst I applied it to my acquired data. Writing of the resultant publication [3] was carried out myself before editing by Miles J. Padgett, Robert W. Boyd and Reuben S. Aspden.

## 3.2 Experimental methods

### 3.2.1 Imaging configurations

In Chapter 2 I provided an overview of the ghost imaging experimental configurations used throughout this body of work. With minor physical adjustments it was possible to reassemble this system into two additional imaging systems which were termed; heralded imaging and direct imaging. These configurations differed in their placement of the object under investigation and by the method which the camera's intensifier was triggered as can be seen in figure 3.1.

To avoid confusion the nomenclature of the "signal" and "idler" arm of the apparatus shall be maintained. In ghost imaging (GI), the object was placed in the signal arm and the camera was triggered externally by the signal from the heralding detector. Although our images are said to be acquired with photons which do not interact with the object 1.2, the same could be said for more mundane examples, a shadow etc. this system allows the imaging of an object in transmission, reflection and diffraction all with low background and high resolution due to the strength of the quantum correlations. The heralded imaging (HI) configuration differed by the placement of the object, it was situated in the idler arm and was directly imaged to the camera, which was again externally triggered by the heralding detector. The camera was therefore triggered for each detected signal photon but the image consisted of only those photons which were transmitted by the object. For comparison images were also acquired in the direct Imaging (DI) configuration, where the object remained in the signal arm and the camera was triggered using its own internal mechanism, at the same rate which the heralded detector triggered in the HI configuration. The image acquired consisted of a subset of photons which passed through the object and by chance arrived during the intensifier's timing window. It is pertinent to point out that regardless of the object's placement, it remained in an image plane of the camera when viewed in the Klyshko AWP.
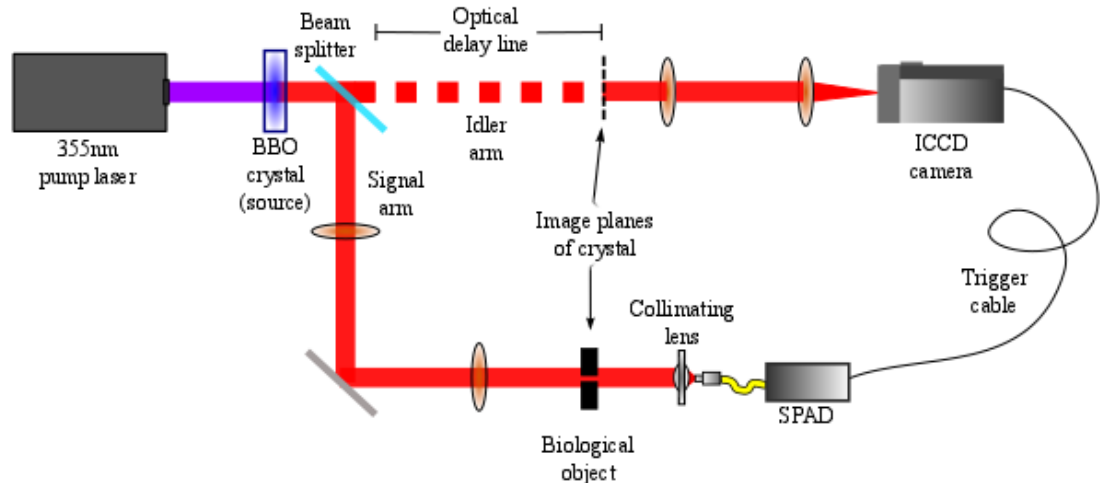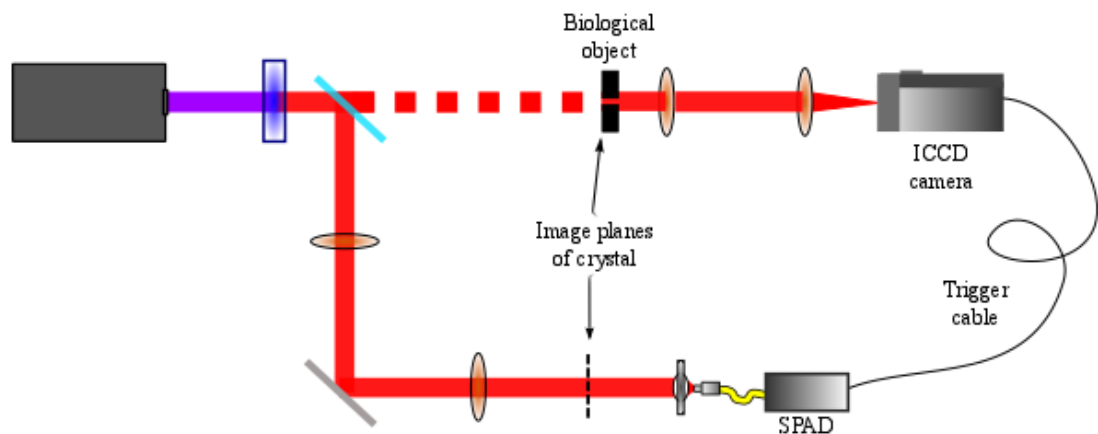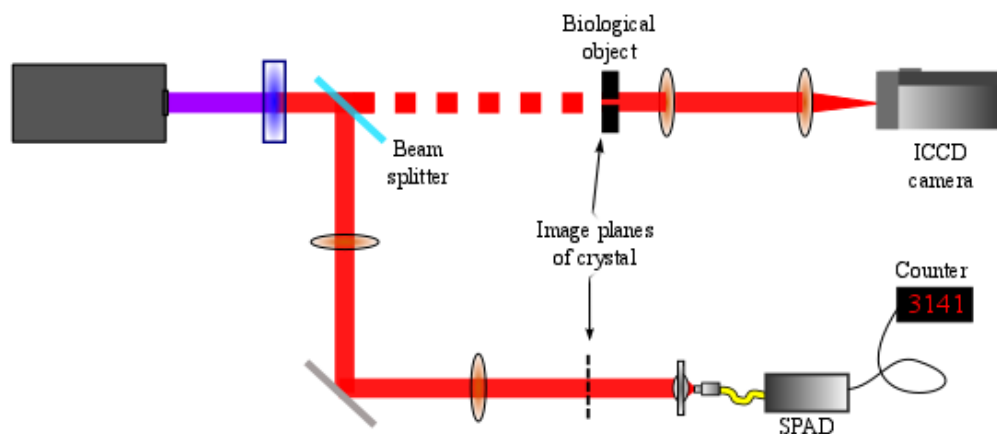
FIGURE 3.1: **Schematic diagrams of imaging regimes. (a) Ghost imaging:** The object was placed in the signal arm and the ICCD was triggered by the heralding detector. **(b) Heralded imaging:** The object was placed in the idler arm and the camera was again triggered by the heralding detector **(c) Direct imaging:** The object was placed in the idler arm and the camera was triggered by its internal trigger mechanism with the trigger rate set to the counts from the heralding detector. To account for electronic delay the idler photons were made to propagate through a 22 m image-preserving free-space delay line.

### 3.2.1.1 Optimum configuration

For each configuration a United States Air Force (USAF) test target was imaged in order to determine which provided the most resolvable images for reconstruction. Figure 3.2 displays a microscope image of the USAF test target used to characterise our imaging configurations and Figure 3.3 shows the images obtained in each imaging configuration. A clearly resolvable image was obtained for both the GI and HI configurations. Defining the contrast, C, as

$$C = \frac{I_{max} - I_{min}}{I_{max} + I_{min}}. \tag{3.1}$$

both GI and HI had a contrast of $\approx$0.7. That obtained in the DI configuration was somewhat less resolvable, with a calculated contrast of $\approx$0.2.

The drop in contrast present in the DI configuration was due to the repetition rate of the laser and periodic nature of the camera's intensifier trigger being entirely uncoordinated. As such, the arrival of a down-converted photon and the firing of the intensifier very rarely coincided and the coincidence nature of the system was lost, resulting in a very low detection efficiency.

At the time of carrying out this investigation [3] it was believed that, at higher flux rates, the GI configuration would prove advantageous over the HI. This assumption was based on the fact that an object placed in the signal arm would reduce the trigger rate, hence reducing the technical demand on the ICCD. Adhering to this conjecture, the following section on image reconstruction was carried out using data obtained in the GI configuration. During the experiment which will be discussed in chapter 6, a clearer understanding of the subtle differences between configurations was gained, showing that in certain circumstances the HI configuration would exhibit benefits beyond GI. A discussion pertaining to these advantages will be postponed to the relevant chapter, in order to emphasize our progressive understanding of the technique.
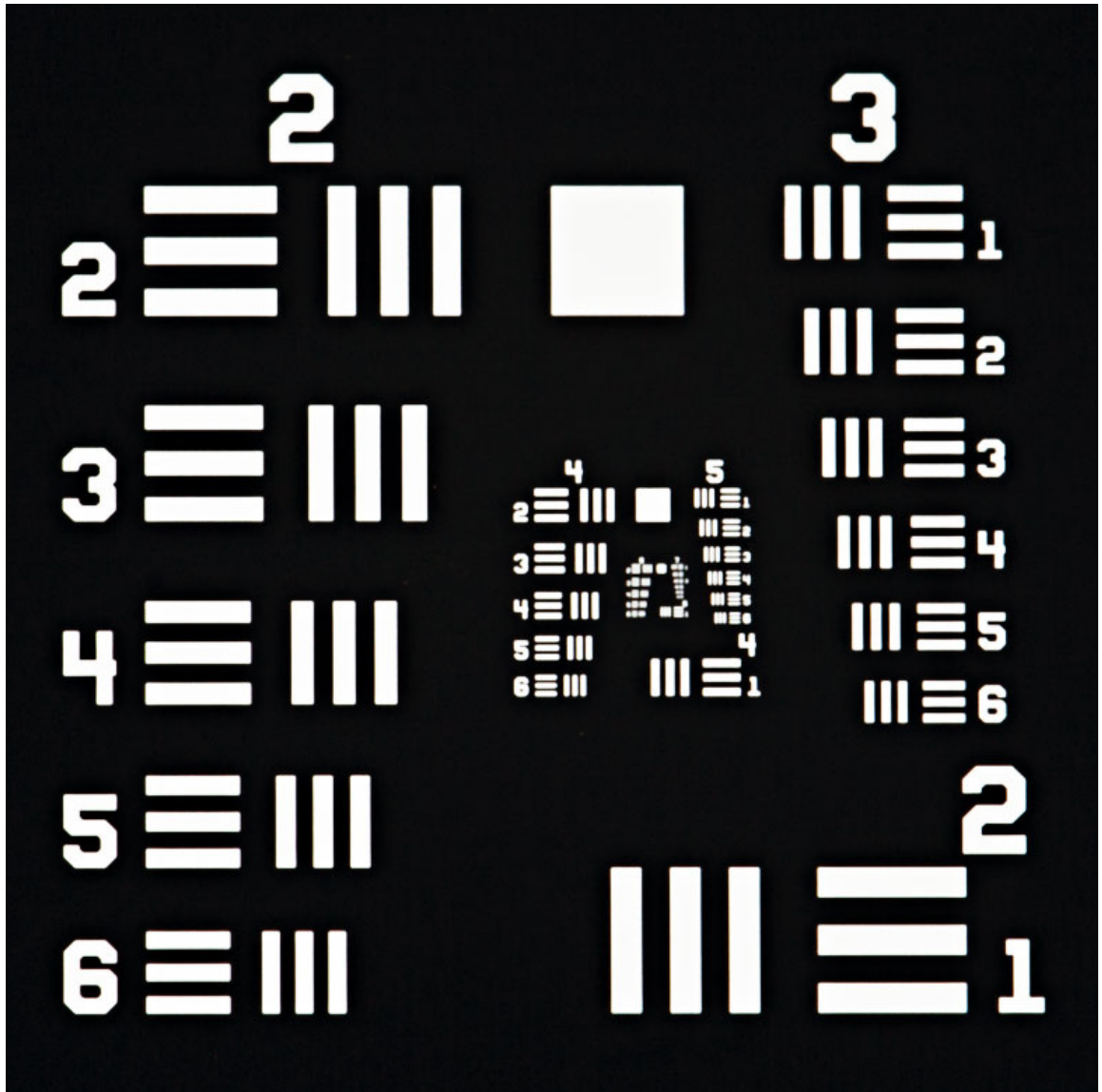
FIGURE 3.2: **United States Air Force test target** Microscope image of the USAF test target used to characterise the systems various imaging configurations.

## 3.3    Image reconstruction

### 3.3.1    Image compression

At the heart of our reconstruction algorithm is the well established principle of digital image compression [46–48], which was first developed to cope with the increasing data deluge of the modern world. How can the amount of information in a data set be reduced (for storage, transportation etc.) whilst maintaining fidelity to the original? This is possible

FIGURE 3.3: **Comparison of images acquired using different imaging regimes.** Cross sections were taken along the dotted lines. **(a) Ghost imaging:** Object placed in signal arm and ICCD triggered from heralding detector. **(b) Heralded imaging:** Object placed in idler arm and ICCD triggered by heralding detector. **(c) Direct imaging:** Object placed in idler arm and camera triggered internally. Resolvable images with high contrast were acquired in (a) and (b) whilst the random triggering in the direct imaging regime resulted in a high background.
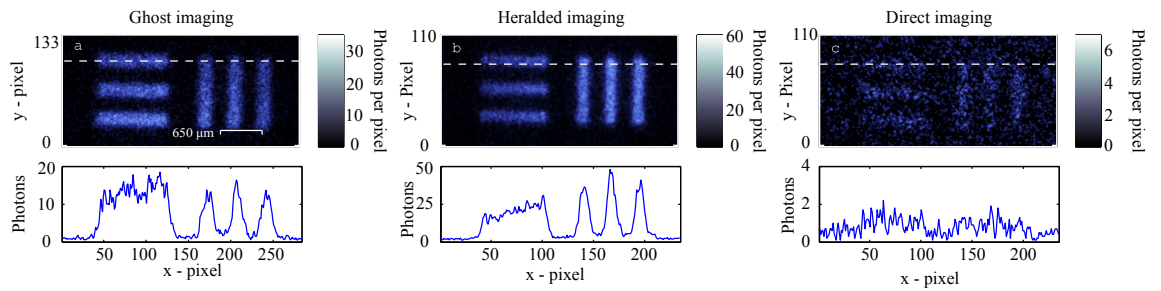
by representing the data in a basis in which it is sparse and removing its most redundant components. The process of finding the optimally sparse basis to perform this compression can be computationally demanding. For most natural scenes there is one such basis which is widely applicable, the spatial frequency domain. Not only are most natural scenes sparse in this domain but the discrete cosine transform (DCT) used to transform it is also computationally simpler, hence faster, than more optimised bases. For instance, observe the image presented in figure 3.4(a). The image is mostly comprised of large swathes of the same intensity such that on a pixel to pixel scale there is little variation. Large areas of constant intensity are described by low spatial frequencies and conversely areas of rapid variation, by high spatial frequencies. This is more clearly displayed in figure 3.4(b) where the image has been transformed into the spatial frequency. The bottom left corner has a cluster of bright pixels which represent the abundant low spatial frequencies. The remainder of the image has few bright pixels containing the high spatial frequencies, clearly demonstrating the aforementioned sparsity in this domain. If one were supplied with these separate spatial frequencies and recombined them from most to least prevalent, one could begin to decipher the scene with comparatively fewer frequency components compared to the original image. This is the foundation of image compression such as JPEG [49], where an image is broken down into smaller blocks which are then transformed into the spatial
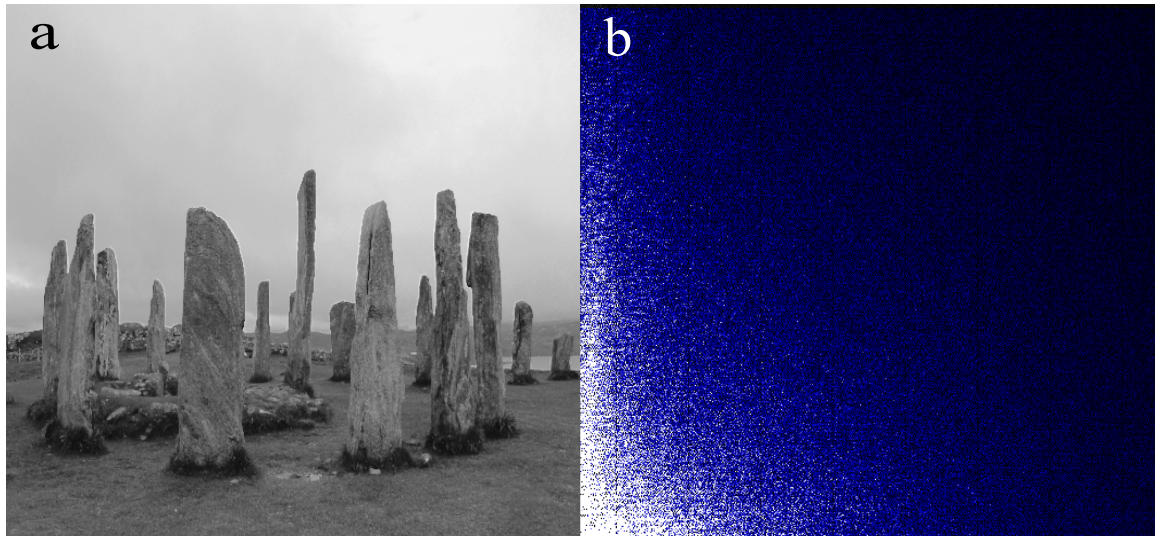
FIGURE 3.4: **Spatial frequencies. (a) Callanish standing stones:** Large areas with very little pixel-to-pixel variation. **(b) Contributing spatial frequencies.** Bottom left to top right represents low to high contributing spatial frequencies in x and y. The cluster of bright points shows the abundant low spatial frequencies with increasingly sparse contributions from higher spatial frequencies. This sparsity is typical of most natural images.

frequency domain and have their more redundant components removed. The result is an image containing fewer spatial frequencies, hence reducing its size in respect to information, yet it remains relatively unchanged to the human observer.

One could employ this logic a stage earlier in order to reduce the time taken to record the image by pre-emptively applying this compression through a technique known as compressive sampling. If one had *a prior* knowledge concerning the contribution spatial frequency compenents in a scene one could record them in order, from most to least prevalent. This would result in the acquisition of an image with fewer measurements than stated by the Nyquist sampling limit [46–48, 50]. This limit states that to resolve an image, one must record at least as many measurements as there are pixels in the final but assumes random sampling.

The following compressive reconstruction technique operated on the same principles as image compression but in reverse. Objects were purposefully under-sampled by randomly recording photons from the object, acquiring fewer spatial frequencies components than

could realistically resolve the image. Artificial photons were then added to the object to increase the images sparsity in the spatial frequency domain. The changes made to the image were restricted to those which maintained a level of fidelity to the original data. Through determining the correct balance between these to criteria, it was possible to reconstruct resolvable images from far fewer measurements than stated by the Nyquist sampling limit.

### 3.3.2 Image reconstruction

This section shall outline the compressive reconstruction technique used to acquire images from under-sampled data. The first term in our reconstruction algorithm provides a measure of how far the data has departed from the originally acquired data. For every image pixel, $N$, we denoted the number of measured photons to be an integer, $n_j$, and the intensity of each modified image pixel to be $I_j$. Given a dark count per pixel of $\varepsilon$ the Poissonian probability distribution of measuring n photons given a pixel intensity, I, was

$$P(I_j; n_j) = \frac{(I_j + \varepsilon)^{n_j} e^{-(I_j + \varepsilon)}}{n_j!}, \qquad (3.2)$$

From this we defined the log likelihood [24] of a modified image as

$$Ln\mathcal{L}(I_j; n_j) = \sum_{j=1}^{N} n_j Ln(I_j + \varepsilon) - (I_j + \varepsilon) - Ln(n_j!), \qquad (3.3)$$

With no additional knowledge, maximising for this term would simply return the original image as $I_j = n_j$. However, given that we know the acquisition process was subject to Poissonian noise, there is a large number of plausible images from which this data could have arisen. Within this landscape of possible images we sought that with the most sparse spatial frequency contribution.

In order to determine the sparsity of the data it was transformed into the spatial frequency domain through the applications of a discrete cosine transform, $\text{DCT}_p(I_j)$. The DCT was chosen for its superior information compaction, i.e. for most typical signals a DCT will

express its frequency components with fewer coefficients than alternatives such as the fast fourier transform (FFT) [51].

By defining the coefficients of the spatial frequencies as $a_i$, we achieved a measure of the sparsity through the number of contributing spatial frequencies within the image, in what we termed the participation function:

$$DCT_p(I_j) = \frac{(\sum |a_i|)^2}{\sum |a_i|^2}.$$ (3.4)

Without changing the the number of photons in an image, this value would increase as the photons were arranged to give an increasing number of spatial frequencies and would reach a minimum when the image could be expressed by a single contributing spatial frequency. The function will lean towards maximising the contribution of whatever the most prevalent spatial frequency component was in the original data. As low spatial frequencies contribute more in most natural images, this term tends to produce a smoothing effect as it removes the less prevalent higher frequencies. However the sparsity promoting nature of the term would have a different subjective effect given an image with an atypical spatial frequency composition. For example, an image containing no large scale structure and a high noise level would become noisier as the higher spatial frequencies would be promoted.

These two factors were then combined into what we termed our merit function, $\mathcal{M}$, defined as

$$\mathcal{M} = Ln\mathcal{L}(I_j, n_j) - \lambda \times DCT_p(I_j).$$ (3.5)

Where $\lambda$ was a balancing factor used to weight the iterative maximisation of this function towards either the original data or the sparsity condition.

The iterative process was carried out by performing a random change to the intensity value of a pixel, $I_j$, which itself was chosen at random. The merit function was then calculated and the process repeated iteratively until the image corresponded to a maximisation of this

merit function. If $\lambda$ was set to a very high level the reconstructed image corresponded to a uniform distribution represented by a single spatial frequency. However, if set to zero the reconstructed image exactly matched the original data. For each image the algorithm was applied to the exact value of $\lambda$ was chosen by subjective judgement of the results, however the subset of suitable values was reduced for each image processed. Though for different scenes the optimum value would be subtly different, any *a prior* knowledge of the object under investigation would allow for a more suitable, initial value of $\lambda$ to be set.

## 3.4 Results

The system was used in the GI configuration to image a household wasp's wing, placed in the signal arm of the system. Each image was comprised of the accumulations of an increasing number of frames and hence an increasing number of photons. The varying number of frames were acquired in order to gauge the effectiveness of the reconstruction for various levels of data-sampling.
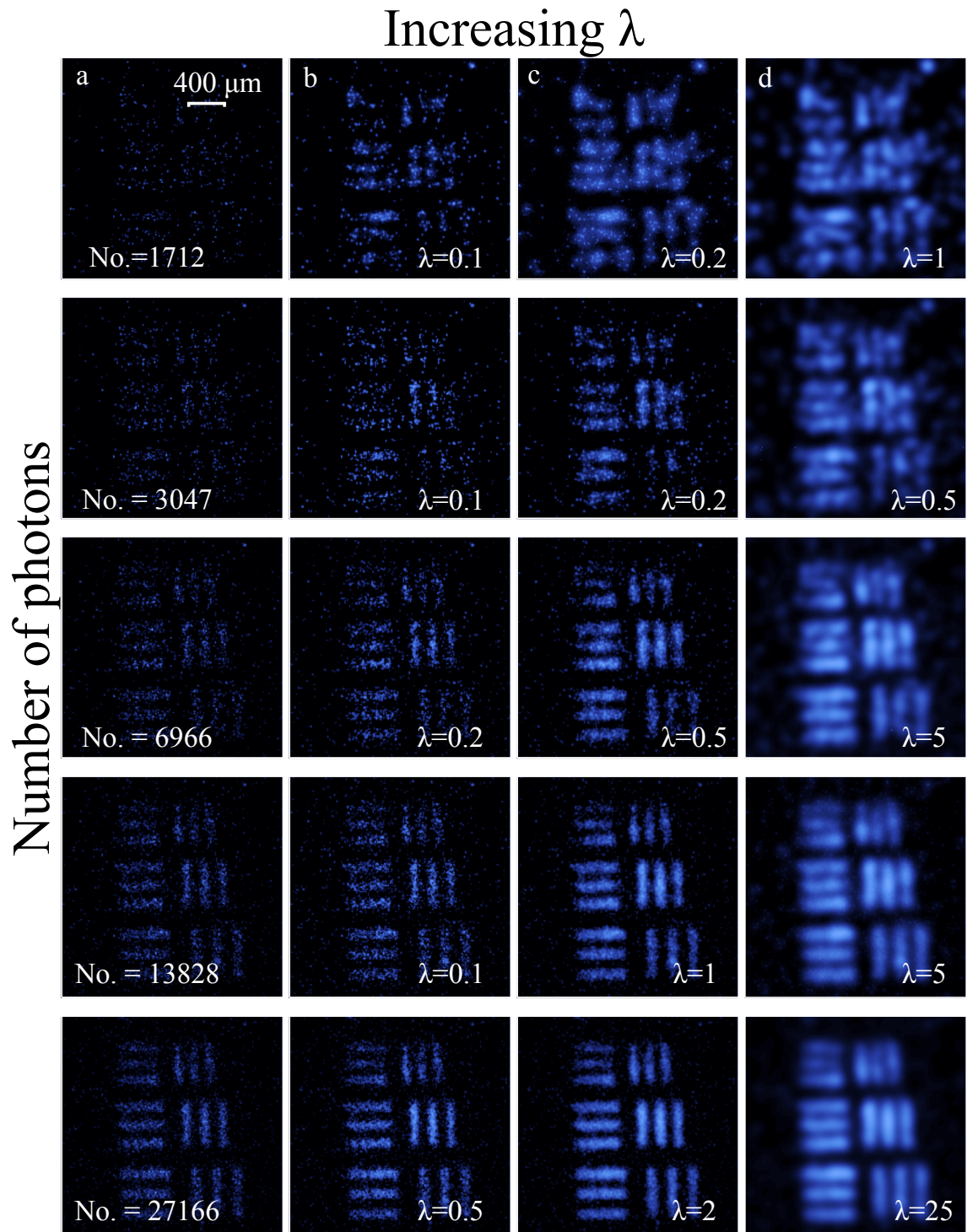
FIGURE 3.5: **Regularised images of a USAF test target.** (a) Original data containing an increasing number of photons. (b) Reconstructed images weighted toward maximising the log likelihood. (c) Reconstructed images with weighting factor balanced to give subjectively best images. (d) Reconstructed images weighted towards maximising the sparsity of spatial frequencies.

Each image was optimised whilst employing different values of $\lambda$. In order to match the resolving power of the optical system to the size of pixels in our ICCD, the images were spatially summed such that a 600x600 pixel image from the ICCD was processed as a 300x300 pixel image. This also reduced computational demand of the reconstruction, hence reduced its time. Figure 3.5 shows images of a USAF test target containing a varying number of photons, reconstructed for varying values of $\lambda$. These highlight the trade-off between the log likelihood and the participation of spatial frequencies within the merit function. For lower values of $\lambda$, the images maintain their fidelity to the original data at the expense of any improvement. At higher levels of $\lambda$, the images became overly smoothed with the associated loss of fine detail. For the data containing many photons the reconstruction appeared to provide a simple smoothing effect to the images. However, for the images containing very few photons the reconstructions true effect was more pronounced. As it promoted the contributing spatial frequencies within the image, it reconstructed the underlying structure of the object. As can be seen in the figure we were able to reconstruct an image of the test target from an acquired image containing only $\approx$7000 photons, corresponding to only 0.2 per image pixel.

Having characterised the system, I then sought to demonstrate its applicability to the imaging of photo-sensitive biological samples. Images were acquired of a household wasp wing and were subjected to our reconstruction process, the results of which are shown in figure 3.6. The resolvable image containing the least number of photons contained only 40,419 photons detected over 90,000 image pixels, which corresponded to <0.5 photons per pixel.
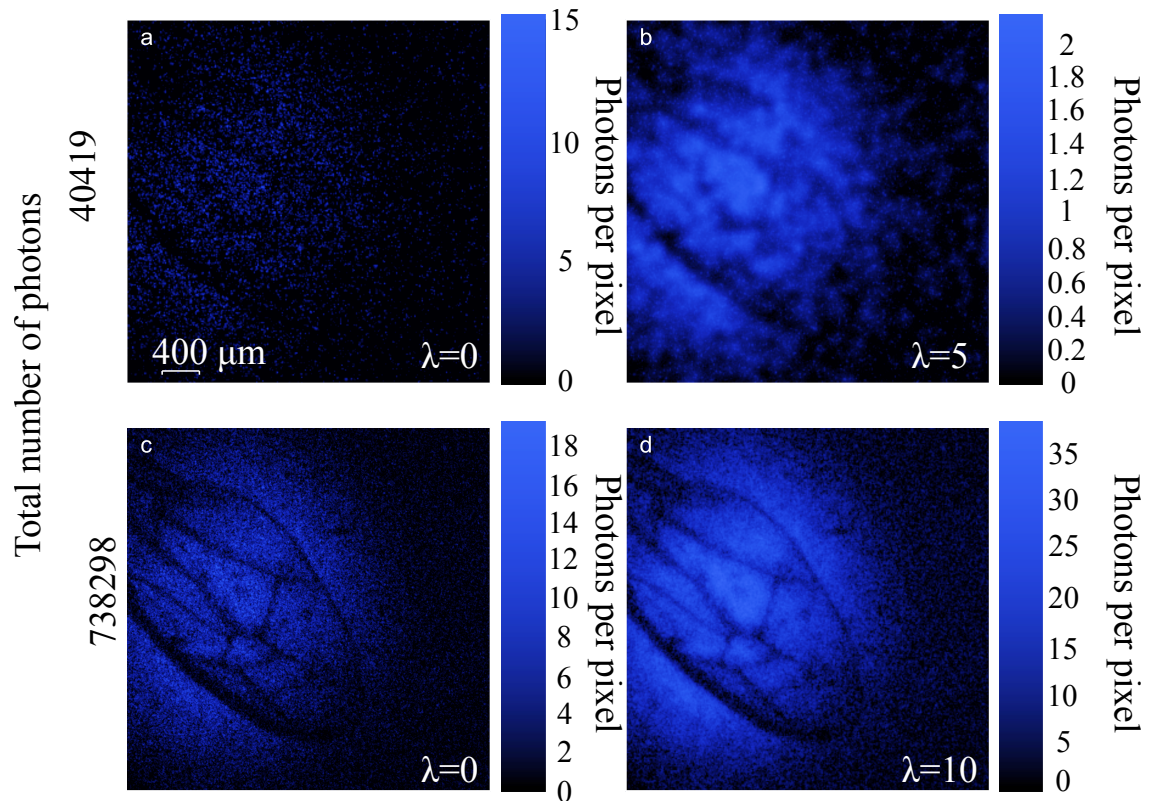
FIGURE 3.6: **Reconstructed low-photon images of a weakly-absorbing object**
(**a**) Image of a household wasp's wing containing 40,419 photons and (**b**) its
reconstruction. (**c**) An image of the wasp wing with a greater number of captured
photons and (**d**) its reconstruction.

## 3.5 Conclusion

Here I have presented a low-photon imaging regime where images have been acquired from
the correlations between down-converted photons, using a time-gated camera. The system
was characterised in different configurations in order to determine which was best suited
for acquiring low-photon images. Knowledge of images natural sparsity in the spatial
frequency domain and the Poissonian nature of their acquisition was used to develop an
image reconstruction technique which required very few photons. As a display of its possible
biological imaging applications, images of a household wasp's wing were reconstructed from
data containing on average fewer than one photon per pixel. This technique could prove

beneficial in biological imaging applications where bleaching may occur at high flux or in sensing of photo-sensitive materials.

Concerning the question posed at the beginning of this chapter I have shown that it is possible to acquire images of an object using far fewer photons than pixels within the image [3]. Through the implementation of our compressive-inspired reconstruction technique to our low-light ghost imaging system, I have acquired images of a biological sample containing only $\approx$7000 photons, bellow what is predicted necessary by the Nyquist sampling theorem.

One could be forgiven for questioning the significant benefits of applying this to a ghost imaging system as opposed to a traditional imaging technique. The following chapter will expand upon this work and show how the heralding nature of this imaging technique may be performed with non-degenerate wavelengths such that an object is illuminated by lower energy photons, undetectable by traditional silicon based cameras.

# Chapter 4

# Trans-wavelength ghost imaging

## 4.1  Introduction

It was shown in the previous chapter that the photon flux incident upon an object under investigation could be greatly reduced, whilst maintaining the fidelity of the acquired images. Reducing the number of photons incident upon an object inherently reduces the energy absorbed by said object. In this chapter I shall address the question; "can this energy deposition be further reduced?" One option for reducing this energy would be to operate our ghost imaging system at a lower energy wavelength such as the short-wave infrared. However, obtaining images of the same quality using infrared illumination gives rise to its own difficulties. Due to the advancements made to silicon semiconductor technology over the last century, photo-detectors based upon silicon technologies are widely prevalent and affordable. However, silicon based detectors are ineffective at wavelengths longer than 1 $\mu$m

---

This chapter contains material published in the following paper:

1  <u>P. A. Morris</u>, R. S. Aspden, J. E. C. Bell, R. W. Boyd, and M. J. Padgett, "Imaging with a small number of photons",
*Nat. Commun*, 6(5913), 2015.

2  R. S. Aspden, N. R. Gemmell, <u>P. A. Morris</u>, D. S. Tasca, L. Mertens, M. G. Tanner, R. A. Kirkwood, A. Ruggeri, A. Tosi, R. W. Boyd, G. S. Buller, R. H. Hadfield and M. J. Padgett, "Photon-sparse microscopy: visible light imaging using infrared illumination"
*Optica*, 2(1049-1052), 2015.

and as such, single-photon sensitive, large array detectors based upon materials sensitive to infrared prove comparably costly.

This challenge was circumvented using a property of our correlated photon source mentioned in Chapter 1. It is possible to cut a BBO crystal such that it produces entangled photons far from degeneracy, i.e. signal and idler possessing drastically different wavelengths whilst maintaining their correlated state. This chapter shall present a variation of our ghost imaging system which utilised one such source to produce signal and idler photons in the near infrared and visible spectrum respectively[52]. As before the signal photon is incident upon the object before its detection by a single-pixel detector whilst the idler propagates to a spatially resolving detector triggered by the former. The silicon based heralding detector was replaced by another single-pixel detector sensitive to the infrared spectrum. This detectors pixel was composed of an indium gallium arsenide/Indium phosphide (InGaAs/InP) chip and was far less costly than a multi-pixel array of the same material. As in the previous chapter, the spatial information was retrieved by a traditional silicon based ICCD camera. This resulted in an imaging system which was capable of transferring spatial information acquired by infrared illumination into the more readily accessible visible spectrum. Not only did this reduce the energy deposited on samples but also provided information not available with visible wavelength illumination. Low-light imaging with infrared light such as this affords many applications, from security to biological imaging as well as the ability to image through substances opaque to visible light such as silicon, which visible detectors are based on. Although possible with different approaches, that shall be discussed, the experiment that follows is the first to utilise such disparate correlated wavelengths, with our object being probed by infrared photons at 1550 nm whilst capturing 460 nm photons with our silicon camera sensor.

### 4.1.1 Contributions

A international team of researchers from the University of Glasgow, Heriot-Watt University, the University of Ottawa, the University of Rochester, The Federal University of Rio de Janeiro and the Polytechnic University of Milan collaborated on the work reported in this

chapter. At the onset of my studies this experiment was under way in a previous iteration conceived by Robert W. Boyd, Gerald S. Buller, Robert H. Hadfield and Miles J. Padgett. The first iteration utilised a superconducting nanowire single photon detector (SNSPD) designed colaboratively by the groups of Robert H. Hadfield and Michael G. Tanner, operated by Nathan R. Gemmell. The experiment was first constructed by Reuben S. Aspden and Daniel S. Tasca. The second iteration of the system replaced the SNSPD with an infrared SPAD designed by the group of Alessandro Ruggeri and was set up by Alberto Tosi. The gold layered silicon objects imaged in the experiment were supplied by Robert A. Kirkwood. Design and construction of the second iteration system was carried out by myself and R. S. Aspden whilst Nathan. R. Gemmell orchestrated the timing circuits. Analysis of the data was carried out by R. S. Aspden and myself and the data reconstruction carried out using my algorithm presented in the previous chapter 3.3.2, which was updated by Lena Mertens. The resulting publication [52] was written by Reuben S. Aspden, Nathan R. Gemmell and myself before editing by Miles J. Padgett, Robert W. Boyd and Gerald S. Buller.

## 4.2   Background

In the past there have been several different approaches to imaging with infrared illumination. Infrared microscopy has achieved high-contrast imaging through the use of structured illumination [53], where the illumination is applied with a known pattern. This has also been demonstrated in our own group, through the masking of images combined with a single-pixel detector [54]. These techniques inherently require high levels of illumination in order to differentiate their signal from a large background, whereas our goal was to minimise the flux a sample experiences. The technique of wavelength upconversion has also been adapted to acquire infrared-information in the visible spectrum but again, requires levels of illumination unsutiable for our proposed applications. Conceptually the reverse of our approach, the technique illuminates the object with infrared photons which are then upconverted, i.e. two infrared photons combined to produce one of higher frequency in the

visible spectrum. Unfortunately this process has an inherently low conversion efficiency and the excitation power required to achieve near unity conversion efficiency generates extreme levels of background noise, hence lower resolution [55–57]. There has been evidence this limitation can be somewhat circumvented with the use of ultrashort pump pulses, providing the neccessary excitation power whilst also reducing the background noise due to its lower, average power [58].

In 2014 Lemos *et al.* [34] demonstrated an innovative technique, based upon induced coherence without induced emission [27], in order to transfer spatial information between wavelengths. In their experiment, infrared idler photons from two separate SPDC sources were overlapped such that they became indistinguishable. The object was placed in one idler path whilst both signal beams were sent through an interferometer. Whenever the object caused absorption in an idler path, the source of idler photons became distinguishable and a visible image was formed at the interferometer output. Their system inherently relied upon the precise overlap of the two beams and required an extremely high photon flux to resolve an image above the noise floor of the system. Seeing as we primarily sought a reduction in energy deposition upon our samples, the method developed by Lemos *et al.* though intriguing, was not applicable to our objective.

## 4.3   Experimental methods

Figure 4.1 shows a compressed schematic of the experiment. The down-conversion source consisted of the same JDSU xcyte laser at 355 nm as discussed in Chapter 2 which was collimated to a size of 470 $\mu$m at FWHM before entering a 1 mm thick BBO crystal. The crystals phase-matching differed from that used in other sections as it was cut to produced signal and idler photons at 1550 nm and 460 nm respectively. These beams were separated using dichroic beam splitter which reflected light at <460 nm with an efficiency of $\approx$95% and transmitted $\approx$90% of light at 1550 nm. The two beams were sent on spatially separate optical paths. High transmission, interference filters were used to select the down-converted light and remove any remaining pump. Some of this residual pump light was sent to a diode,
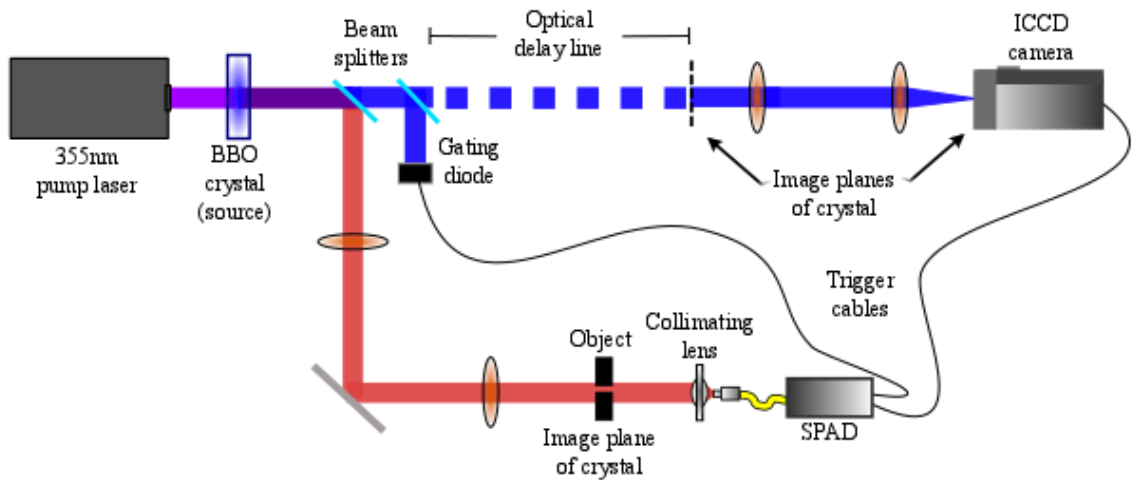
FIGURE 4.1: **Simplified schematic of non-degenerate ghost imaging system:** Non-degenerate signal and idler photons produced through SPDC were separated by a cold mirror. Residual pump photons were used to gate the heralding detector. The 1550 nm signal photons were incident upon an object before their detection by the SPAD, which triggered the ICCD. The 460 nm idler photons propagated through the 25.2 m image-preserving free-space delay line to the ICCD camera where their spatial distribution was recorded.

the signal of which was sent to the SPAD such that an extremely short gate (1.4 ns) could be synchronised to the pulsed source, reducing the rate of false detections.

The 1550 nm signal photons were imaged to the plane of the object with a magnification of M=-1/2 with the transmitted light being re-imaged to the plane of the detector with a magnification of M=-10. The detector used was a free-space coupled InGaAs/InP SPAD [59] with a quantum efficiency of ≈25% and a dark count rate of <1 kHz. A square detection area of 625 $\mu$m$^2$ and a high NA (≈0.7) lead to its high detection efficiency.

The 460 nm idler beam was re-imaged through the optical delay line to the spatially resolving ICCD camera with a magnification of M=5. The imaging system in the AWP had an effective magnification of M=-10 from the SPAD to the camera. The total electronic delay from a detection at the SPAD to firing of the ICCD intensifier was approximately 75 ns, therefore the image preserving delay line was 25.2 m in length with any disparity in timing adjusted for by the internal DDG.
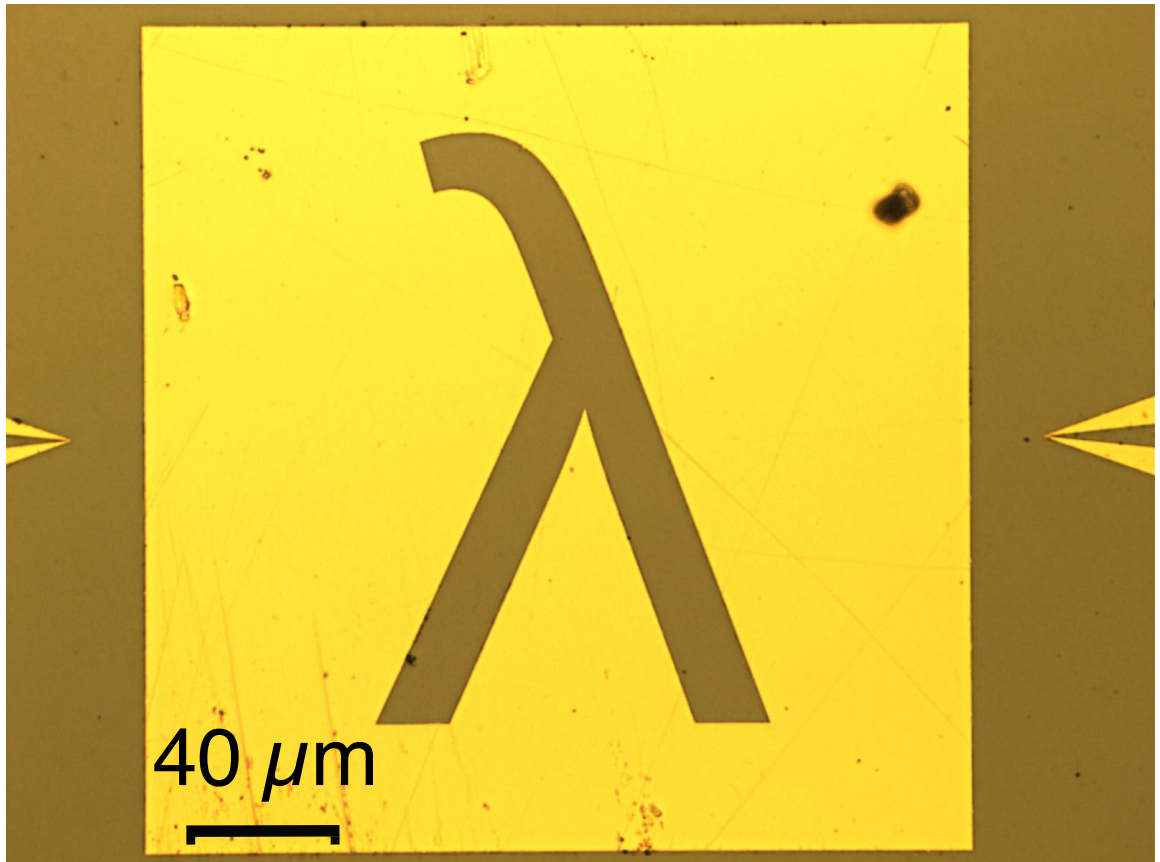
FIGURE 4.2: **Microscopic image of object under investigation:** 120 $\mu$m tall Greek letter Lambda etched into a gold layer deposited onto a 387 $\mu m$ thick, polished silicon wafer.

## 4.4   Image acquisition

To highlight the infrared imaging capabilities of the system objects were chosen which were entirely opaque to visible illumination. These were microscopic lettering etched by electron beam lithography on to gold deposited upon 387 $\mu m$ thick, polished silicon wafers (created by Robert Kirkwood of the James Watt Nanofabrication Centre). A traditional microscope image of the objects is shown in figure 4.2 for reference, the lettering being 120 $\mu$m within a bounding box of 160 $\mu$m. At the signal wavelength of 1550 nm the gold was opaque whilst the silicon was transparent. Any visible photons which were not filtered out of the signal arm were fully absorbed by the object whilst any infrared light in the idler arm was undetectable by the ICCD camera, being out with its photo-cathodes spectral range.

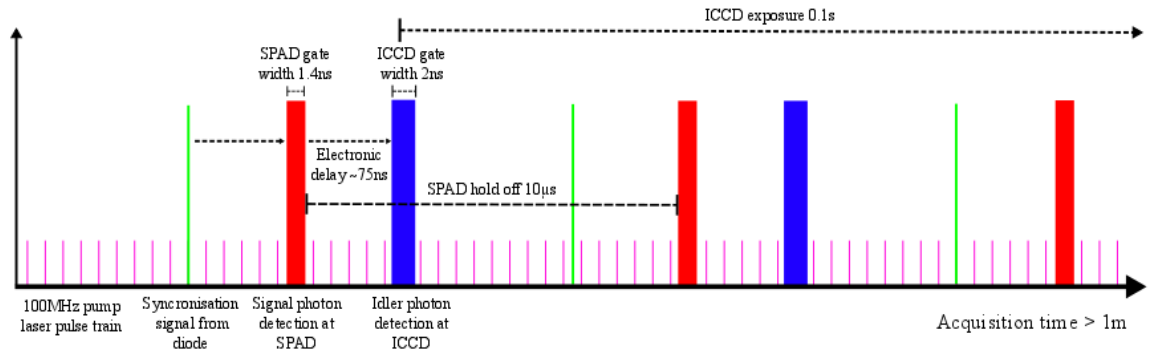FIGURE 4.3: **Acquisition timings** Pulses are generated every 10 ns by the UV pump laser and residual pump light is detected by a photodiode. This signal is used to synchronise the SPAD to the pump pulse train, allowing a short gate time of 1.4 ns. The detection of a signal photon at the SPAD triggered the ICCD intensifier with a electronic delay of 75 ns, heralding the arrival of the correlated idler photon. The triggering allowed for a short gate width of 2 ns during which the intensifier fires. To avoid after-pulsing the SPAD had a hold-off time of 15 $\mu$s over which it could not detect signal photons. Timings shown are a representation and are not to scale.

The time gating of the intensifier (10 ns) and source characteristics ($\approx$50 mW average power at 150 MHz from the pump) ensured the camera detected, on average, no more than one photon per triggering of its intensifier. The trigger rate of the intensifier was $\approx$10 kHz with an exposure time of 0.1 s such that the camera triggered many times per captured frame. For a visualisation of the timings involved, see figure 4.3 If these were the only factors then each trigger of the camera would yield a photo-event, however this efficiency was limited by the throughput of the optical system and the quantum efficiency of the camera, leading to an efficiency of $\approx$5% in the idler arm. This resulted in each frame containing <100 photons but as there were $1024 \times 1024$ pixels, there is on average less than one photon per pixel per frame. This allowed us to apply our photon counting methodology described in Chapter 2 converting each frame into photons per pixel. These were then summed to give our final images containing known numbers of photons.

The rate at which our images were acquired involved many efficiency factors in the system, from the optical efficiency of both arms to the quantum efficiency of both detectors as well as the pair generation rate of our correlated photons. As has been outlined throughout, this pair generation rate could not be arbitrarily increased without degrading our image quality due to the coincidence nature of our system. In this particular experiment the

pair generation rate was approximately $10^6$ photon pairs second. The free-space coupled InGaAs/Inp SPAD used as the heralding detector in this system had a large detection area ($25\mu$m)and high NA ($\approx$), leading to a high coupling efficiency. The detector had the disadvantage of a high dark count rate ($\approx$9,000 CPS) and a maximum trigger rate limited by the hold off time-off time between detections, which was necessary to avoid after-pulsing effects. This was slightly offset by the ability to operate the detector in gate mode, triggering it off of residual pump light such that it was synchronised with the source pulses. This allowed for a 1.4 ns gate duration, reducing the rate of false idler detections.

## 4.5 Results
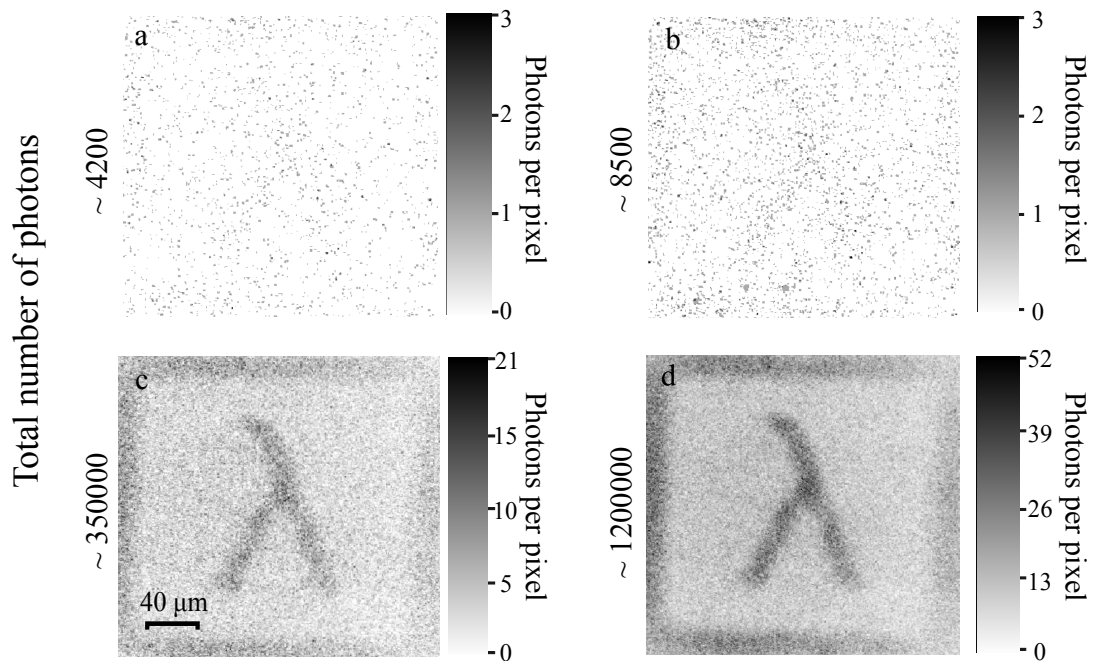


FIGURE 4.4: **Trans-wavelength ghost images:** Images of a Greek letter lambda etched into gold layered on a polished silicon wafer. Images were acquired with an increasing number of visible photons whilst the object was probed by IR photons.

Figure 4.4 shows images of our object over an increasing number of accumulated frames and hence an increasing number of captured photons, all of which were captured with 0.1 s exposures of the intensifier. Many of these frames were combined giving total exposure times ranging from 8 *seconds* to 40 *minutes* reaching a contrast of $\approx$82% in 4.4(d). When

considering low-light imaging, the number of photons captured by the camera is not the pertinent measurement but the number of photons incident upon the sample. The number of photons detected by the heralding detector with no object in the path was measured, as was the number of photons detected with an object present in the beam path. With these two values and the quantum efficiency of the detector it was possible to infer the number of photons incident upon the object under investigation. The number of photons incident within the 160 $\mu m^2$ gold boundary box visible in figure 4.2 to be $\approx 2 \times 10^5$ photons per second. Given these photons were at 1550 $nm$ the illumination power was calculated as $\approx 25$ $fW$ with an energy deposition of $\approx 16$ $nJcm^{-2}s^{-1}$.
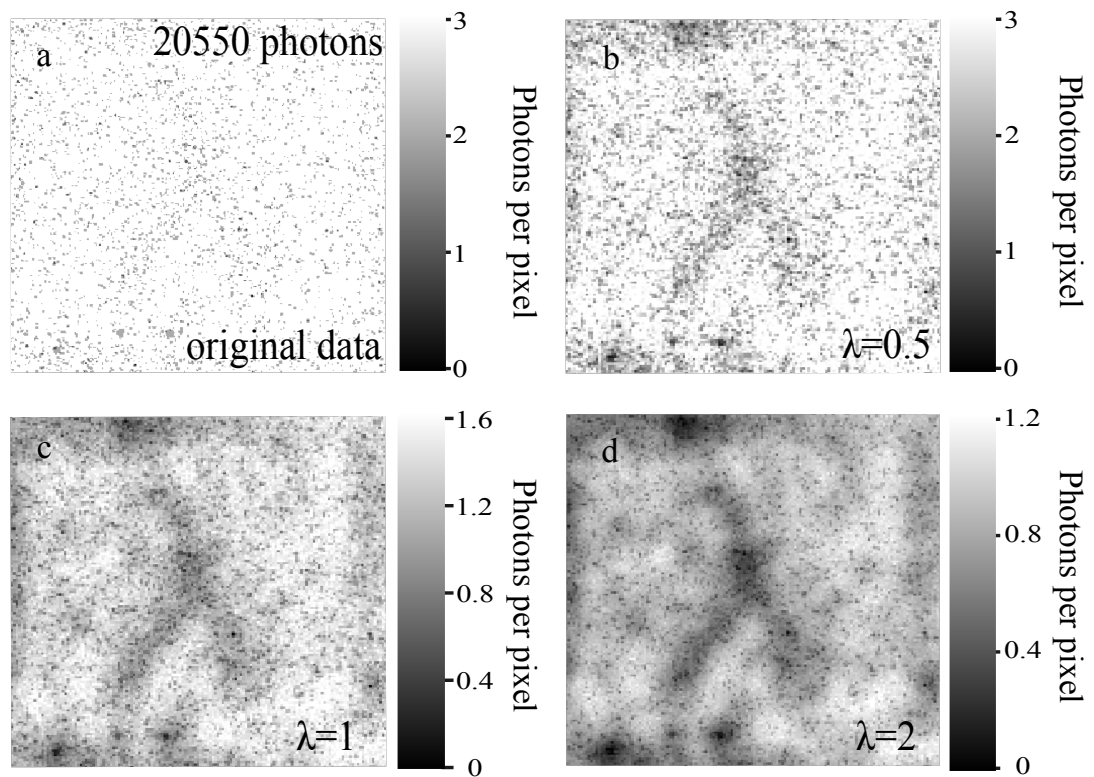


FIGURE 4.5: **Regularised trans-wavelength images:** Images of the same lambda presented in 4.4 which have been processed by our compressive reconstruction algorithm 3.3.2 with optimised balancing factors ($\lambda$). **(a)** Original data.**(b-d)** reconstructions with an increasing weighting towards sparsity in the spatial frequency domain.

It is clear in figure 4.4 that there is a trade-off between reducing the energy deposition on the object at the expense of reducing the image quality. However, this can be compensated for using the reconstruction technique introduced in Chapter 3 to iteratively reconstruct

images of subjectively higher quality using the equation derived in the previous chapter 3.3.2:

$$\mathcal{M} = Ln\mathcal{L}(I_j, n_j) - \lambda \times DCT_p(I_j). \tag{4.1}$$

Figure 4.5(a) shows data acquired from the summation of 100 frames containing $\approx$20550 photons and its reconstructions over a range balancing factors, $\lambda$.

## 4.6 Resolution

In order to estimate the resolution of the system the point spread function of the optical throughput was determined by analysing a knife edge transition between gold and silicon. The deconvolution of this transition with a step function revealed a Guassian point spread function (PSF) in the object plane of 2PSF$\approx$15 $\mu$m. Although affected by many factors [10, 30], our resolution is fundamentally limited by the strength of the position correlations between signal and idler combined with the fidelity of the imaging optics. This is taken as the standard deviation, $\alpha_x$, of the strength of the position correlations in the plane of investigation [32, 60, 61]:

$$\alpha_x \approx MA\sqrt{\frac{L_z\lambda_p}{\pi}}, \tag{4.2}$$

where M is the magnification from crystal to the plane of measurement, L is the transverse length of the crystal, $\lambda_p$ is the pump wavelength and A is a scaling factor dependant on the approximations used in deriving the formula, taken as $\sqrt{0.455}$. This resulted in a position correlation of 5 $\mu$m in the plane of our object. Although our system could approach this value, there was an obvious disparity between this and our measured resolution, which was contributed to the fidelity of the relay optics. Given the magnification of the system and a numerical aperture of the heralding detector of 0.7, we estimated our coupling efficiency to be $\approx$50%. Increasing this value with a larger area detector and/or higher NA would bring

us closer to the fundamental resolution limit, however the SPAD employed here was at the cutting edge in terms of both these factors. A further investigation into the resolution limits of Ghost imaging and factors which lead to its degradation is presented in Chapter 6.

## 4.7 Conclusion

As a response to asking "can the energy deposition on a sample be reduced during the imaging process?" I have presented an infrared imaging system capable of reducing this factor through its ability to transfer spatial information between wavelengths[52]. Microscopic images of objects totally opaque to visible light have been acquired from infrared illumination at 1550 nm whilst recording them via correlated visible photons at 460 nm. This was the largest frequency difference displayed by a quantum ghost imaging system. The ability to image in the infrared has allowed us to reduce the energy deposition on our samples to $\approx 16\ nJcm^{-2}s^{-1}$. during imaging, far below that utilised in standard live-cell imaging techniques [62]. Typically the photoxicity level for standard live-cell imaging is taken from the solar constant, i.e. the average energy deposition on the surface of the Earth by the Sun[63] estimated as $\approx 0.1\ Wcm^{-2}$. In practice this value is dependant upon several factors including the illuminating wavelength and nature of the source (i.e. pulsed or continuous) as well as the specific structures under investigation. As a large proportion of light from the sun is emitted in the infrared, this was taken as an adequate gauge of our systems abilities.

This is certainly a positive response to the question stated at the beginning of this chapter however these decreased levels of energy deposition came at the expense of image quality. The time frame necessary to acquire high quality images imposes severe limitations upon our system, which produced images with a quality scaling with exposure time. Due to the triggering nature of our ghost imaging system the illumination cannot simply be increased to reduce the acquisition time but any improvements must arise through reducing the inefficiencies of the system.

The research presented thus far has focussed on reducing the energy impinging upon samples under investigation by ghost imaging. This has naturally led us to pursue its applicability to biological imaging, where samples such as live cells are often photosensitive [63]. In many areas of biological imaging, such as microscopy, samples under investigation often present additional difficulties such as partial or total transparency to illuminating wavelengths[64]. The following chapter shall investigate how ghost imaging can offer an improvement over the current approaches to imaging microscopic, transparent objects.

# Chapter 5

# Phase-contrast ghost imaging

## 5.1 Introduction

The experiments presented thus far have demonstrated the low-light capabilities of our ghost imaging system. I have shown the techniques applicability to imaging biological samples, where objects often display photo-sensitivity [62, 63]. In many cases biological objects are transparent in the visible spectrum and as such, a traditional intensity image offers little structural information [64]. The light passing through a transparent object does, however, experience a phase shift due to the varying refractive indices of the material. It is possible to retrieve structural information through the technique known as phase-contrast imaging, first demonstrated by Fritz Zernike in 1942 [64], commonly employed in microscopy and x-ray imaging [65], which shall be outlined below. This chapter shall present an experiment which applied phase-contrast imaging techniques to our low-light ghost imaging system in order to determine any advantages it can offer over traditional methods.

---

This chapter contains material published in the following paper:

- R. S. Aspden, <u>P. A. Morris</u>, He. Ruiqiung, Q. Chen and M. J. Padgett, "Heralded phase-contrast imaging using an orbital angular momentum phase-filter",
  *Journal of Optics*, 18(055204), 2016.

The technique of phase filtering employs filters which alter only the phase of light without altering the intensity distribution, in order to retrieve structural information from light transmitted through an opaque object. The phase steps present within the transmitted beam can be enhanced in a variety of forms through the use of such filters. The chosen phase filter is placed within the Fourier plane of the object, either in the source of illumination or in the subsequent imaging optics. The group of Ritsch-Marte *et al.* [66, 67] demonstrated a particularly advantageous phase filter, which could achieve isotropic edge-enhancement, i.e., all phase steps within the object are enhanced regardless of their orientation. This phase filter is known as a spiral-phase filter, aptly named for its ability to impart orbital angular momentum (OAM) to light [68], endowing it with helical phasefronts [69]. Rather than implement a physical, transmissive spiral-phase plate we opted to display its holographic counterpart on a spatial light modulator (SLM). This was composed of diffraction grating combined with a forked singularity [70]. This afforded more freedom, allowing us to align the the filter and change its location within the experiment without the need to physically interact with the system, at the expense of the components efficiency.

As opposed to conventional phase imaging the following experiment utilised the OAM correlations present between down-converted photons to perform non-local phase filtering of acquired images i.e. the phase filter was applied to a spatially separate beam than that illuminating the object.

### 5.1.1 Contributions

The work carried out in this chapter was carried out by three researchers within our group in collaboration with a visiting researcher from Nanjing University of Science and Technology. Miles J. Padgett suggested the experiment with input from Qian Chen, which was carried out by myself with help from Reuben S. Aspden. He Ruiqiung carried out an supporting experiment which simulated our experiment with the klyshko model. Reuben S. Aspden and I analysed the acquired data and wrote the subsequent publication[71] which was edited by Miles J. Padgett.

## 5.2   Background

There are additional caveats to performing phase-contrast imaging which do not apply when performing classical intensity imaging. These arise from the techniques reliance upon the diffraction of light from the phase filter and object. In any standard diffraction experiment, to acquire a high contrast diffraction pattern, the illuminating source must be coherent [72]. If illuminated with a incoherent source, many diffraction patterns would be produced, reducing visibility. In our ghost imaging system this spatial coherence was not achieved via the illumination source but rather was enforced by the spatial selectivity of the heralding detector. This is understandable through the Klyshko model discussed in Chapter 1, where the heralding detector takes the place of the illumination with light propgating backward through the system, essentially becoming a classical experiment. Studies into the effects arising from the spatial selectivity of the heralding detector have been previously published [41]. In the system presented here this was easily controlled through the choice of fibre coupling to the heralding detector. Where high contrast intensity images were recorded, a multi-mode fibre was coupled to the detector and when we sought the diffraction pattern produced by the object, this was replaced by a single-mode fibre [24].

When imaging a transparent object, areas of constant refractive index are viewed as areas of constant intensity. This is due to the light passing through acquiring a constant phase shift across the area such that constructive interference occurs between each path. Where there is a phase discontinuity resulting from a step in the refractive index, the opposite occurs. The light on either side of the step acquires a different phase shift and destructively interferes, resulting in a line of reduced intensity, the contrast of which depends upon the phase difference between the paths. This is illustrated in figure 5.1. With the spiral-phase filter placed in the far-field, each point in the image plane possessed helical phase-fronts [66]. This then results in areas of constant phase destructively interfering as each path interferes with its neighbour, which is $\pi$ out of phase at the boundary. The same reasoning suggests any area containing a refractive index step is imaged as a line of increased intensity as there is constructive interference at the boundary. Unlike other phase filters which offer

edge-enhancement along a single axis, the nature of the spiral-phase filter results in isotropic edge-enhancement, as can be seen in figure 5.1. This is not only true for phase shifts of $\pi$ but can enhance steps as small as $0.005\pi$ which would be entirely unresolvable without phase-contrast methods[66].
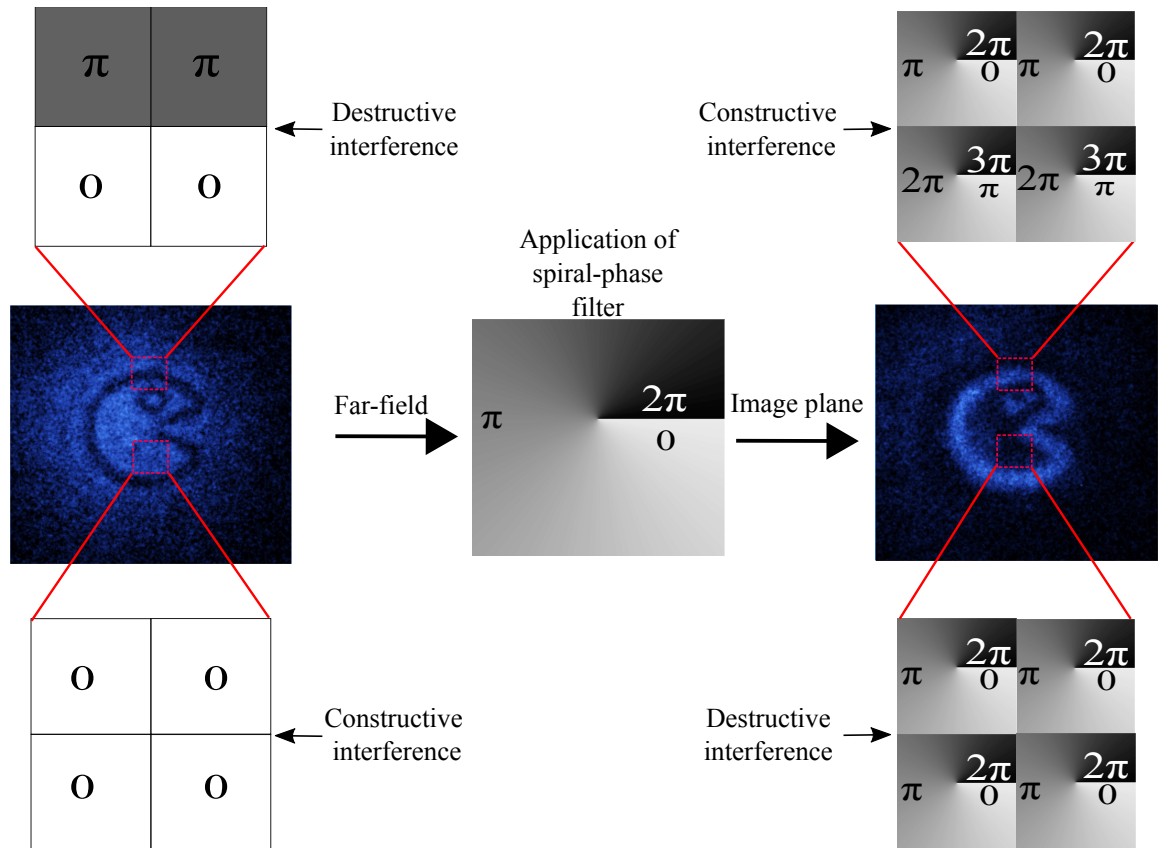


FIGURE 5.1: **Spiral-phase filtering** From left to right: A beam is incident upon a phase-only object (see figure 5.2 insert). The dark lines within the image are caused by destructive interference along phase discontinuities whilst bright areas are a result of constructive interference. Regions of interest above and below show the phase distribution of each of these areas. In the far-field the beam carrying the image is incident upon the phase filter, endowing OAM to each photon. In the following image plane, the phase steps constructively interfere giving lines of increased intensity whilst the areas of constant phase destructively interfere. Again this can be seen in the phase distribution within these areas. The total intensity of the image remains unchanged as only the phase is altered.

## 5.3   Experimental methods

Figure 5.2 shows the experimental phase-contrast ghost imaging set-up. Degenerate down-converted photons at 710 nm were produced by a 3 mm long BBO crystal which was pumped by a collimated beam with a diameter of 0.5 mm at FWHM, in a similar set up as that presented in Chapter 3. The large pump diameter ensured strong correlations over a wide range of spatial positions [6]. Once separated from the idler beam at a polarising beam splitter (PBS) the signal photons were imaged onto a spatial light modulator (SLM) encoded with a phase-only hologram, a phase-object combined with a diffraction grating to select only the light interacting with the SLM. Both arms of the system had a magnification of $M = 3$ from crystal to detector such that the phase object was illuminated by a spatially incoherent beam with a diameter of 1.5 mm. The refelcted photons diffracted into the first order of the SLM diffraction grating were then detected by the heralding detector. This was comprised of a microscope objective lens with a magnification of 20 and a single-mode fibre coupled to a SPAD. This detector had a trigger rate of approximately 1800 counts per second (CPS) and dark count rate of 1200 CPS. As discussed in the previous section this single-mode selectivity was necessary to acquire high contrast phase-contrast images[41]. Upon detecting a photon the heralding detector sent an electronic signal to trigger the intensifier of the spatially resolving ICCD camera in the idler arm. During this time the idler photon was imaged to the camera via a second SLM placed in the far-field of the crystal and camera, which was encoded with a phase filter combined with a diffraction grating. The gate width of the intensifier, the time which the intensifier fired for, was set to 4 ns, essentially eliminating any uncorrelated photons from the image [9]. As with our previous experiments the pump beam was also attenuated to ensure no more than one correlated photon pair was produced per pulse of the laser.

In this implimentation of phase filtering the object and phase filter were positioned in separate optical paths such that no light interacting with the object interacted with the phase filter. Although not the first ghost imaging system to display non-local phase filtering
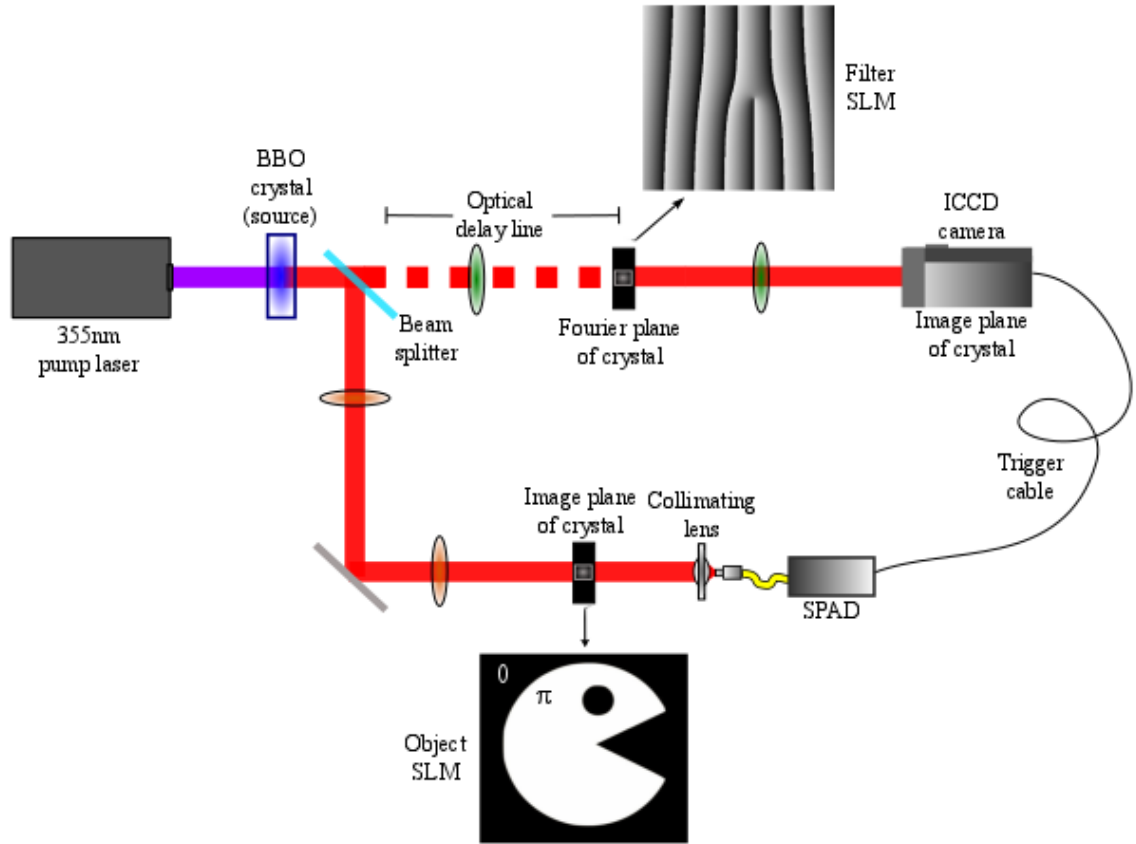
FIGURE 5.2: **Simplified schematic of phase-contrast ghost imaging system:** Correlated photons produced by SPDC within a BBO crystal were separated at a beam splitter. The signal photons were incident upon an SLM, placed in an image plane of the crystal, which displayed the phase-only objects. These were then detected at the SPAD, the signal from which triggered the ICCD. The idler photons passed through a 22 m optical delay line to account for electronic lag in the triggering mechanism, then were incident upon a second SLM placed in the far-field of the crystal which endowed them with OAM through the use of a spiral-phase filter. They then had their spatial distribution recoded by the ICCD, also placed in an image plane of the crystal.

[24], this was the first demonstration utilising a camera to capture images across the full field of view of the object.

## 5.4 Results

In figure 5.3(a-f) we see the images of our phase-only object accumulated with an increasing number of frames. As in the previous iterations of our ghost imaging system, the beam

forming the images was spatially separate from the object. With the idler-arm SLM displaying a plane-wave filter (a simple diffraction grating) the triggered images exhibited areas of decreased intensity where the phase-steps within the object were situated. Conversely the areas of constant phase within the object constructively interfered resulting in areas of higher intensity. With the encoding of a spiral-phase filter upon the idler-arm SLM the contrast of the images was inverted 5.3(d-f). The phase-steps then exhibited isotropic edge-enhancement despite the object and filter never being illuminated by the same photons. Significantly, as only the phase of both signal and idler were altered the images contained a similar number of photons.

Although the filtered and unfiltered images containing a large numbers of photons, 5.3(c+f), an analysis revealed the average contrast to differ. The unfiltered image, 5.3(c), displayed a contrast of $\approx 58\%$ whereas its isotropically edge-enhanced counterpart, 5.3(f), increased to $\approx 67\%$. For the images containing fewer photons, 5.3(a+d), the object was only clear when the idler beam was spiral-phase filtered. This would allow the identification of phase objects an order of magnitude quicker when employing a spiral-phase filter as opposed to standard phase-contrast imaging. This edge-enhancement effect would be more pronounced when applied to minute phase-steps ($0.005\pi$) which would be unresolvable in an unfiltered image[66].

The benefits of performing the phase filtering process non-locally are non-trivial due to the high timing resolution of the ICCD camera and the strong time correlations of the photons. During the acquisition of the image containing $\approx 7300$ photons the intensifier only fired for 3.6 ms of the 500 s exposure time with the SPAD detecting 600 photons per second. This is an order of magnitude fewer photons than is required by our system in a non-edge-enhanced ghost imaging configuration, with an exposure time three orders of magnitude faster.

## 5.5   Conclusion

This chapter has extended the repertoire of our ghost imaging system to encompass the edge-enhancement of phase-only objects. This allowed for the acquisition of transparent
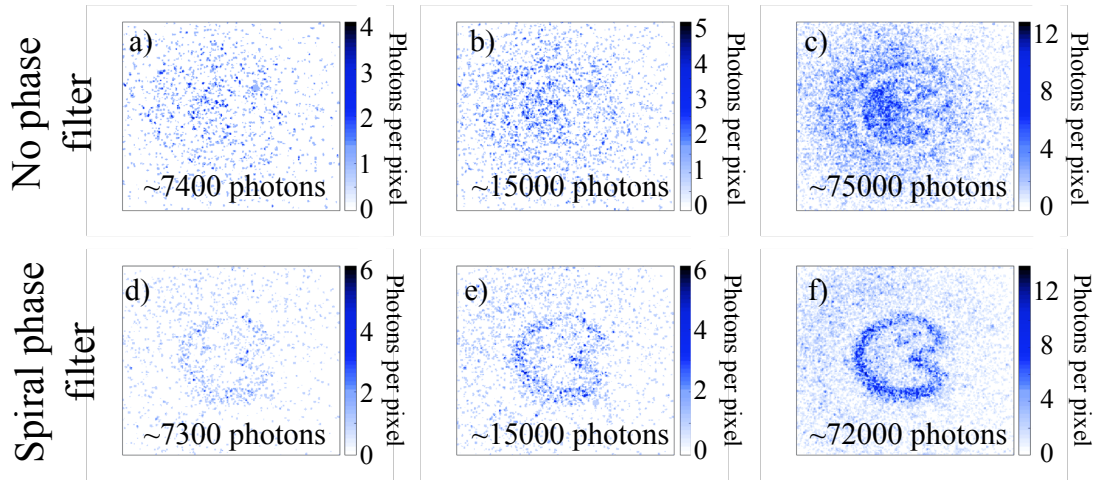
FIGURE 5.3: **Images of phase-only object containing an increasing number of photons. (a-c)** Images acquired with no phase filtering applied to the idler beam. **(d-f)** Images acquired with a spiral-phase filter applied to the idler beam resulting in isotropic edge-enhancement of the objects phase steps.

objects, exhibiting isotropic edge-enhancement. This effect was achieved non-locally with respect to the object by use of a spiral-phase filter placed in the Fourier plane of the camera and down-conversion source. This allowed for the acquisition of resolvable images containing as little as $\approx 7300$ photons. This has further extended the applicability of ghost imaging for the imaging of photo-sensitive objects, affording the ability to image translucent objects by applying the well established tools of phase-contrast imaging. This approach could be operated in tandem to the transwavelength system discussed in the previous chapter to acquire phase information of objects transparent to infrared, such as silicon based microchips.

Each of the chapters presented thus far have investigated the applicability of our ghost imaging system with regards to reducing the energy an object under investigation is exposed to. This has been shown to be possible through; a reduction in the number of photons necessary to form and image, use of lower energy photons and increasing the available information through phase-contrast imaging. These advancements are, however, unable to compete with standard imaging techniques if they are gained at the expense of image quality. The following and final experimental chapter will deviate from this thread in order

to investigate a more fundamental characteristic of our imaging technique, namely the fundamental resolution of ghost imaging and its limitations.

# Chapter 6

# Resolution limits of ghost imaging

## 6.1 Introduction

The preceding chapters have focussed on the benefits of quantum ghost imaging, specifically its ability to drastically reduce the energy deposited upon a sample under different forms of imaging. These benefits, however, become somewhat less impressive if the obtainable images do not match the resolution of standard techniques. This chapter shall present an examination of the resolution limits of quantum ghost imaging and the corresponding effects in ghost diffraction. In conventional imaging systems the resolution is limited by the resolving power of the optics between the object and the imaging detector. In ghost imaging, in addition to this optical resolution limit, the resolution will be shown to degrade when the strength of the spatial correlations generated by the SPDC source are artificially reduced [73].

---

This chapter contains material published in the following paper:

- P. A. Moreau, E. Toninelli, <u>P. A. Morris</u>, R. S. Aspden, T. Gregory, G. Spalding, R. W. Boyd, and M. J. Padgett, "Resolution limits of quantum ghost imaging",
  *Optics Express*, 26(7528–7536), 2018.

### 6.1.1 Contributions

The work discussed in this chapter was carried out in collaboration with several researchers within our group and with the input of Gabriel Spalding and Robert W. Boyd. The material presented here was acquired during my time with the group however the subsequent publication [73] was completed following my departure. Discussions between Gabriel Spalding, Robert W. Boyd, Miles J. Padgett and myself inspired the experiment. I carried out the experimental work and analysed the data which is included here, with aid from Reuben S. Aspden. The work was continued by P. A. Moreau and E. Toninelli after my departure from the group and it is their data which can be found in the publication. The paper was written by P. A. Moreau and was contributed to by myself, E. Toninelli, T. Gregory, G. Spalding and R. W. Boyd.

## 6.2 Background

Quantum ghost imaging and diffraction were initially demonstrated by the group of Shih in 1995 [10]. As discussed in prior chapters, our system has the ability to switch plane that the camera is in with regards to the crystal, allowing access to both position correlations and momentum anti-correlations with ease. In our experimental systems the single-pixel detector has a large detection area, capable of detecting photons across the full field of view of the imaging system; often termed the "bucket" detector. To maximize the collection efficiency the detector must couple many spatial modes, at least one mode for each independent pixel in the image[41]. As when using the Fourier filter in the previous chapter, ghost diffraction required the single-pixel detector to be coupled to just one spatial mode in order to acquire high contrast diffraction patterns [41]. This modal requirement is analogous to the need to use a spatially coherent illumination source in classical diffraction experiments. In addition to ghost diffraction, a single-mode detector also allows ghost imaging but the need to couple many modes means that the coupling efficiency of any one mode is small. In this work a single spatial mode detector was used to allow the experiment to be used in both imaging and diffraction configurations without the need to re-align into

the heralding detector. The ability to display an object on SLMs situated in both signal and idler arm of the experiment 6.2 enabled the direct comparison of ghost imaging and diffraction with their classical counterparts.

This chapter will present an investigation into the resolution of both the image and diffraction pattern of a double slit, obtained in either heralded or ghost imaging configurations. Common to all imaging systems the point-spread function of the camera optics set a limit to the realisable resolution of the acquired image. In heralded imaging, the resolution of the image was set solely by this limit, however in ghost imaging, the situation was more complex. Ultimately, in ghost imaging the resolution of the system could not exceed the resolution with which the spatial correlations between the down-converted photons were created or could be measured. The effective strength of this correlation was therefore limited by a combination of: the resolving power of the optics used to relay the plane of the crystals to that containing the camera, the resolving power of the optics used to relay the plane of the crystal to that containing the object and fundamentally, the underlying strength of the spatial correlations. The disparity between resolutions of a heralded and a ghost imaging system were highlighted by degrading the strength of the spatial correlations in both configurations. This degradation of the spatial correlations was implemented by reducing the diameter of the pump beam in the plane of the down-conversion crystal. It will be shown that when the pump beam was unrestricted in size, the image resolution in the heralded and ghost imaging configurations was the same. However, when the pump beam was reduced in size, although the resolution of the heralded imaging configuration remained unchanged, the resolution of the ghost imaging configuration was degraded. A similar argument applied to heralded and ghost diffraction, with the degraded spatial correlations limiting the number of diffraction orders visible in the ghost diffraction pattern.

### 6.2.1 Correlation width

As stated above, neglecting the limiting factors present in all imaging experiments, the resolution of a ghost imaging system is fundamentally limited by what is known as the
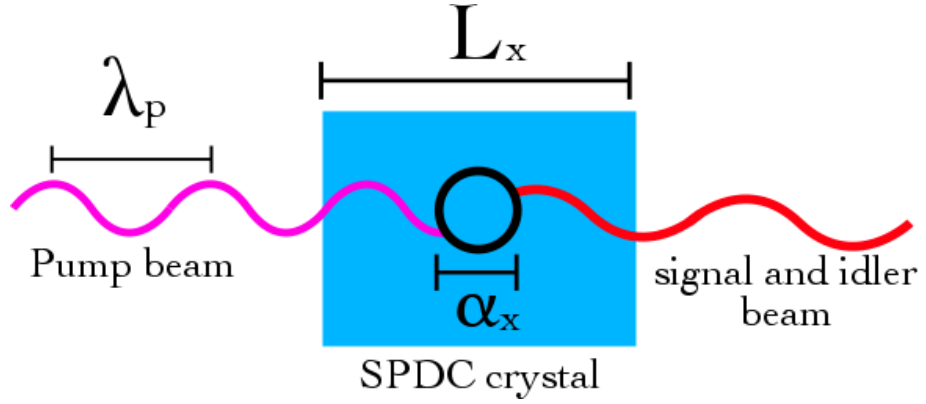
FIGURE 6.1: **Simplified schematic of equation 6.1:** $\lambda_p$ is the wavelength of the pump beam, $L_z$ is the length of the down-conversion crystal along the optical axis and $\alpha_x$ is the transverse coherence length of the entangled photon pairs i.e. the uncertainty in the position of where the correlated photons are produced.

correlation width of the down-conversion process. This width is the area over which down-converted photon pairs are produced in the BBO crystal i.e. the uncertainty in the position in which they are created. This width, $\alpha_x$, has been comprehensively derived[32, 75] to give an approximate of

$$\alpha_x \approx A\sqrt{\frac{L_z\lambda_p}{\pi}}, \tag{6.1}$$

where $L_z$ is the transverse width of the down-conversion crystal, $\lambda_p$ is the pump wavelength and A is a scaling factor, dependant upon the approximations used in the derivation. Figure 6.1 shows a representation of the pertinent factors in equation 6.1

As seen in equation 6.2 this length can be reduced through shortening the length of the crystal, suggesting the possibility of a resolution beating the standard diffraction limit. However, when one considers the propagation of this length through an optical imaging system, the point spread function of the system has to be taken into account. In the image plane of the crystal this width $\alpha_{im}$ is described as

$$\alpha_{im} \approx \frac{f\lambda_p}{\pi w_p}, \tag{6.2}$$

where $f$ is the effective focal length of the Fourier-transforming lens and $w_p$ is the waist of the pump beam in the plane of the crystal. Hence the realisable resolution is fundamentally limited by, not only the intervening optics, but the size of the pump beam used in the down-conversion process measured in the plane of the crystal.

## 6.3 Experimental methods

A simplified and unfolded schematic of the experiment configurations is shown in figure 1 a). This geometry was based on that detailed in 2.3. In summary, the system consisted of a down-conversion source, a single-pixel, single spatial-mode, heralding detector in one arm and an intensified CCD (ICCD) camera in the other arm. As discussed above, the down-converted photons were highly correlated in transverse position and highly anti-correlated in transverse momentum. The down-converted photons were separated from each other into the two arms using a 50:50 pellicle beam splitter. SLMs positioned in the far field of the source (i.e. in the back focal plane of a transform lens) were used to create the object, in either of the two arms. The object was a double slit, with slit widths 100 $\mu$m, and a slit separation of 500 $\mu$m (positioning of the object and camera in the far-field of the source meant that the resulting image was inverted with respect to the object). In the heralding arm, the photon was incident on the SLM that was itself imaged to the heralding detector. The heralding detector was a single-mode fiber coupled to a single-photon avalanche detector (SPAD). The correlated photon was incident on the other SLM (which in this case acted as a mirror) and passed through a free-space, image-preserving, optical delay line before being imaged onto the ICCD camera. The optical delay line again compensated for the electronic delay in the heralding detector and in the ICCD trigger electronics, ensuring that the photon reached the camera at the precise moment that the camera was triggered by the heralding detector (i.e. establishing the $\approx$5 ns coincidence window for all recorded measurements).

For the heralded configuration, the double slit was created on the SLM in the camera arm, the heralding arm simply produced the signal to trigger the ICCD. In addition to studying
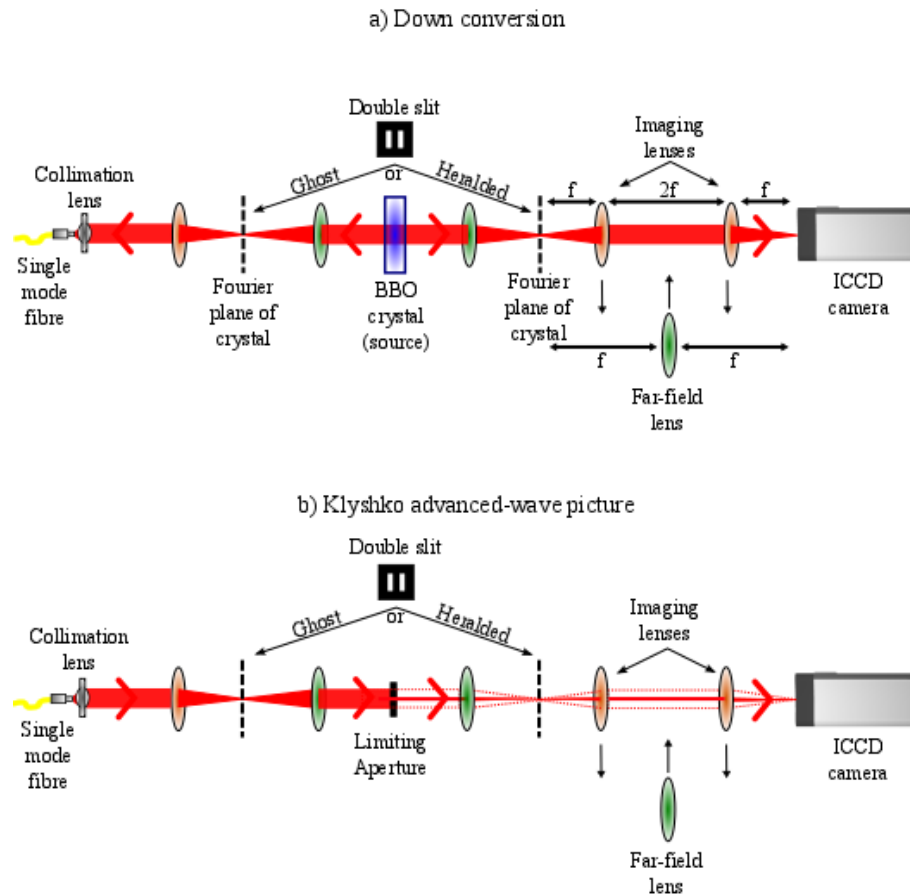
FIGURE 6.2: **(a) Unwrapped simplified schematic of the down-conversion imaging system.**The SLMs, either of which could be programmed to create the object (i.e. the double slits), were in the far-field (FF) of the BBO crystal. Depending upon which SLM was used to create the slit, the configuration was either a ghost or heralded imaging system. Furthermore, an interchangeable lens system was used change the plane of the camera from the image plane to the far-field.**(b) The Klyshko Advanced Wave Picture.** In this representation, the heralding detector was replaced by a classical source propagating through the system. The BBO crystal acts as a spatial filter with the same properties as the pump beam in the down-conversion set up. The process reduces the number of spatial modes in the ghost imaging system, degrading the image resolution and reducing the number of diffraction orders.

image formation we could also use this system to study the diffraction pattern created by the double slits.

To observe the diffraction pattern the plane of the camera relative to the SLMs was changed from the image plane (hence recording an image of the slits) to the far field (hence recording a diffraction pattern of the slits) through the use of an interchangeable lens system located in the camera arm of the experiment (see figure 1).

## 6.4 Results

The resolution of ghost imaging is affected by the strength of the spatial correlations used, manifest as the correlation width over which the photons are produced, which can be smaller than the standard diffraction limit. However, as detailed below, the practically realisable correlation length cannot be smaller than the resolution of the optical system used to measure it[32]. Therefore, in a ghost imaging system, what matters is the strength of the correlation between the photons as measured in the plane of the object with those measured in the plane of the image. The strength of this correlation is limited by the point-spread-function associated with the optics between the down-conversion crystal and object and/or between the down-conversion crystal and camera.

In our configuration both the object and resulting image were in the far field of the crystal (giving an image inverted with respect to the object). The position correlation inherent in the far field of the source was determined by the transverse momentum correlation between signal and idler photons in the down-conversion crystal. The strength of this momentum correlation was set by the transverse momentum uncertainty in the pump beam, which was itself set by the diameter of the pump beam. Consequently, as measured in the far field, the position correlation length between signal and idler photons was given as $\alpha_x \approx f\lambda_p/\pi w_p$ where $f$ is the effective focal length of the Fourier-transform, far-field lens and $w_p$ is the waist of the pump beam. For our experimental configuration and an unrestricted pump beam this gave a correlation length in the plane of the object of $\approx$25 $\mu$m, which in turn limited the maximum resolution of the ghost image.

As mentioned above, the strength of these far-field position correlations and hence the image resolution could be reduced by restricting the size of the pump beam through the introduction of appropriate apertures. Importantly, because the SLMs creating the objects are located in the far field of the down-conversion crystal, reducing the size of the pump beam did not affect the field of view of the image, only the strength of the correlations on which the image formation depends.

We acquired both heralded/ghost images and heralded/ghost diffraction patterns for three different sizes of pump beam; starting with a beam of 900 $\mu$m (large) and then, by using restricting apertures placed into the pump beam, beams of width 450 $\mu$m (medium) and 150 $\mu$m (small). The resulting images in 6.3 show that the resolution in the heralded imaging configuration was largely unaffected by the size of the pump beam, because the resolution does not rely upon the strength of the correlation between the signal and idler photons. By contrast, the same figure clearly demonstrates that in the ghost-imaging configuration the resolution was dependant upon the size of the pump beam and the strength of the resultant correlations. For the largest pump beam the correlations were sufficiently strong that they were not the limiting factor in the resolution of the ghost imaging system and we observed that the ghost imaging had similar resolution to the heralded imaging configuration. For the medium-sized pump beam the correlations were weakened and impacted somewhat on the resolution of the ghost imaging system. The resolution of the ghost imaging system was already less than that of the herald configuration. Finally, for the smallest pump beam, the resolution of the ghost-imaging configuration was sufficiently degraded that the two individual slits could no longer be resolved. This key experimental demonstration of progressive reduction in resolution highlighted the impact of any reduction in the strength of the correlations between the signal and idler photons, as measured in the far field of the down-conversion crystal.

Further increasing the size of the pump beam would strengthen the transverse correlations. Critically, however, no matter how strong the inherent correlations in the plane of the down-conversion crystal, the resolution of the imaging system could not exceed that of the optics between the down-conversion crystal and the object/camera.

Similar considerations apply to the comparison of ghost and heralded diffraction patterns 6.4. When there was no restriction on the pump beam width, the number of diffraction orders in heralded and ghost diffraction was similar. On the other hand, as the size of the pump beam was decreased the number of diffraction orders in the ghost set up was reduced whilst there was no change to the heralded diffraction orders. Further decreasing the width of the pump beam resulted in a total loss of resolvable ghost diffraction orders.
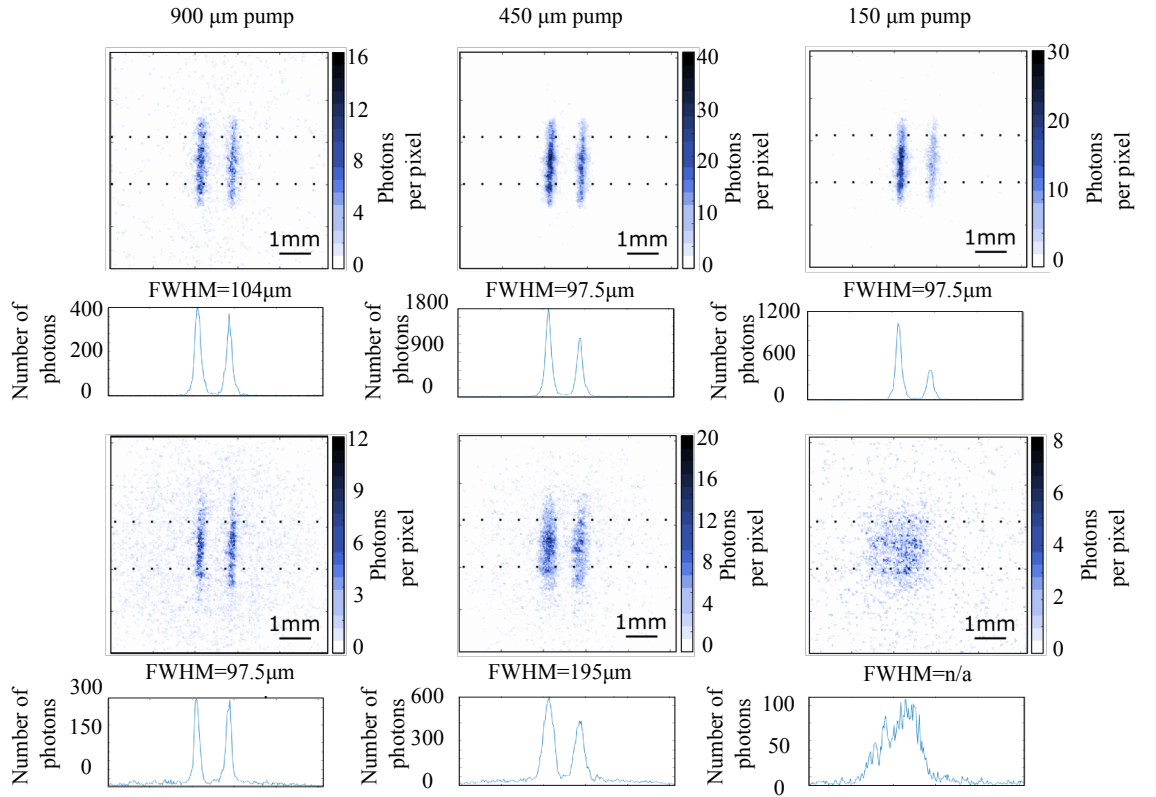
FIGURE 6.3: **Imaging Results:** The first row shows the heralded image and the second row the ghost image for different sizes of the pump beam (900m, 450m and 150m). The cross section at the bottom is the sum of the rows between the dotted lines. The heralded image was largely unaffected by a reduction in the pump size, whereas the ghost image resolution decreased significantly as the modal generation capacity decreased. The full width half maximum (FWHM) is quoted for the largest peak in each image.

## 6.5   Discussion

The differences between heralded and ghost imaging can be understood using the Klyshko advanced-wave picture (AWP) [44, 76], shown in 6.2. In the AWP the heralding detector is replaced with a classical source possessing the same characteristics of the heralding detector (aperture and numerical aperture) and this source back-propagates through the heralding arm to the nonlinear crystal. The front facet of the crystal acts as a mirror and reflects the light back into the camera arm. The intensity distribution measured by the camera is an exact prediction of that which would be detected by measuring the down-converted photons in coincidence with the heralding detector. In the AWP the two SLMs in our system were in image planes of each other, and both were in the far-field of the nonlinear crystal.
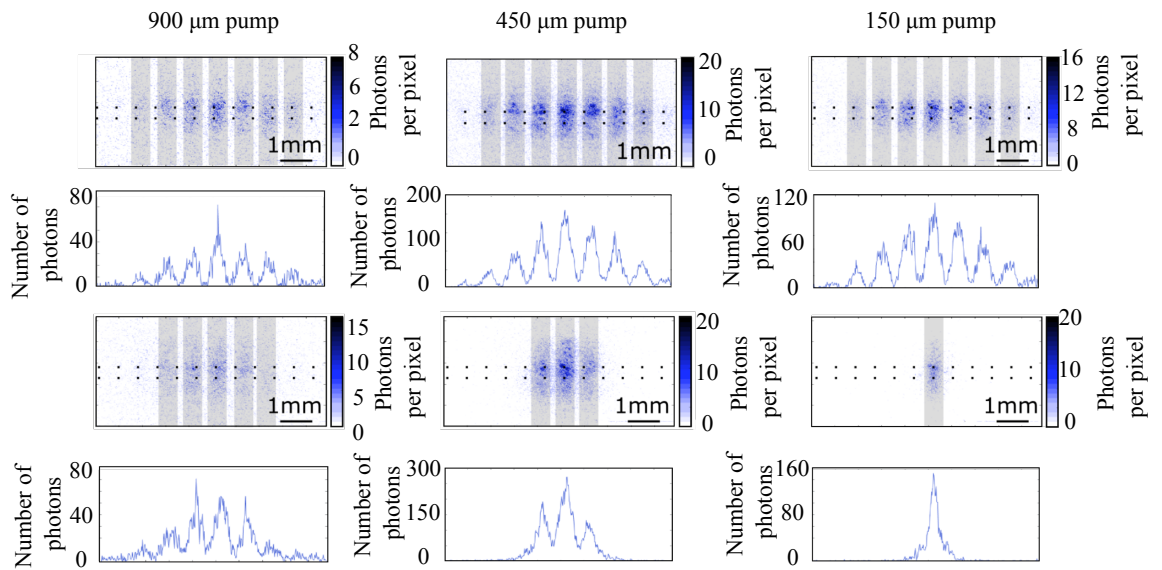
FIGURE 6.4: **Diffraction Results:** The top row shows the diffraction pattern obtained in the heralded configuration and the bottom row the diffraction pattern in the ghost configuration for different sizes of the pump beam (900m, 450m and 150m). Each diffraction order is highlighted in grey. As the pump beam size was reduced, the number of ghost diffraction orders decreased, while there was no change in the heralded diffraction pattern.

As discussed above, introducing an aperture into the pump beam reduced the strength of the spatial correlation between signal and idler photons. In the AWP the aperture in the pump beam is analogous to a spatial filter part way through the imaging system. When the slits are positioned for heralded imaging this spatial filter acts only on the spatial mode of the illumination light and hence has no substantive effect on the resolution of the image. However, when the slits are positioned for ghost imaging, the spatial filter lies between the slits and the camera and hence reduces the resolution of the image. A similar argument applies to heralded and ghost diffraction but within AWP the aperture restricts the field of view of the diffraction pattern and hence the number of observable diffraction orders. The role played by the degree of spatial coherence characterising the illumination source is a subtle but important factor influencing the characteristics of all imaging systems. Although the down-conversion source had many spatial modes, the use of a single-mode heralding detector effectively meant that both the heralded and ghost configurations were equivalent to spatially coherent illumination within the AWP.

Note that in many previous configurations utilized for ghost imaging, including the comparison presented in chapter 3, the heralded and ghost configurations had shown similar resolution. This similarity was because the pump beam was large and thus the resolution of heralded and ghost imaging configuration was in both cases limited only by the resolving power of the optics between the down-conversion crystal and the camera/object.

## 6.6   Conclusion

We compared the resolution of heralded and ghost imaging and discussed the influence of strength of the correlations produced by the down-conversion source and its effect on the image resolution. We showed that whilst heralded imaging and diffraction are independent of the source characteristics, in the ghost configuration the resulting image and diffraction pattern were dependent on the strength of the correlations produced by the down-conversion source. This work is the first experimental demonstration of factors governing the spatial resolution of ghost imaging.

# Chapter 7

# Conclusions

There has been considerable amount of research performed on the possible imaging applications of entangled light. At the forefront of these investigations has been the technique known as ghost imaging, which has fostered many claims surrounding its advantages since its debut in 1995. The ability to probe an object with one set of photons whilst forming an image from a spatially separate set, which never interacted with said object, offers many interesting and often counter intuitive opportunities to gather information. This thesis has demonstrated several experiments which have explored the capabilities and limitations of ghost imaging. I have demonstrated a reduction in the energy deposition upon objects during the acquisition of intensity and phase images in chapters 3 and 5 respectively. A reduction in the number of photons necessary to form an image was shown in chapter 3, through the application of compressive sensing techniques to our low-light ghost imaging system. The energy deposition upon objects under investigation was further reduced in chapter 4 through exposing samples to lower energy, infrared photons whilst acquiring the images in the visible spectrum. The technique was expanded to encompass the imaging of transparent objects in chapter 5, through the application of phase-filtering techniques. In the process I have also determined what limits resolution of ghost imaging in chapter 6, providing an overview of the ensemble of limiting factors at play.

Each of the advancements presented throughout this thesis were achievable primarily due to the non-classical strength of the correlated states produced through the process of SPDC, in addition to the coincidental nature of their detection. With cutting edge intensified CCD camera technology providing nanosecond timing resolutions I achieved a reduction in background noise levels such that individual photons could be identified and counted. This allowed for the precise measurement of the efficiencies involved in each experiment and allowed the estimation of the number of photons that samples were exposed to during the imaging process.

By employing reconstruction techniques inspired by compressive sensing[46–48] I have shown in chapter 3 the feasibility of acquiring images containing fewer photons than pixels in the image. This was achieved by promoting the natural sparsity of most typical images when expressed in the spatial frequency domain. Using this sparsity assumption to add false photo-events to images whilst maintaining their similarity to the original acquired data. Through this I was able to reconstruct high fidelity images of a biological specimen containing on average <1 photon per image pixel. This approach benefited from the Poissonian nature of our single photon detections but is applicable to any imaging regime where minimising the number of acquired photons is beneficial. This experiment provided an answer to the question of "Can an image of an object be reconstructed from fewer photons than pixels in the image?"

The ability to produce down-converted photons at drastically different wavelengths proved an ideal tool to further reduce the flux incident upon an object during ghost imaging by probing it with a far less energetic wavelength of light. In chapter 4 our non-degenerate ghost imaging system was shown to be capable of probing an object with infrared light at 1550 nm whilst acquiring images within the visible spectrum at 460 nm. The IR illumination not only drastically reduced the energy deposition on the object but made details which were opaque to visible light accessible, without the need for a costly spatially resolving IR detector. This allowed for the counter intuitive ability to image through silicon (opaque to visible light) whilst acquiring images on a traditional silicon based camera, only requiring a single-pixel detector sensitive in the IR spectrum. By combining the gains of

this system with those of our reconstruction technique presented in chapter 3 I was able to reduce the energy deposition by three orders of magnitude compared to traditional microscopy techniques. It was our hope to advance the system to the applications stage of cell microscopy, where high intensity illumination can damage samples, however the current time frames intrinsic in the heralding nature of our image acquisition made imaging of live cell processes a goal for the future.

As chapter 4 addressed the possibility of acquiring spatial information from an object entirely opaque to visible illumination I then questioned the converse situation; can we acquire structural information when the object is translucent to visible imaging, such as certain biological material. Although having no effect on the intensity of transmitted light such objects do impose phase shifts across the illuminating field, which can be minute fractions of a wavelength. The field of phase-contrast microscopy provided an abundant catalogue of techniques used to acquire such phase information such as spiral-phase filtering. Applying an OAM filter to a light field containing phase steps results in an isotropic enhancement of those steps, highlighting them within an intensity image. I combined this technique with our previously developed system to acquire ghost images of phase objects displayed on an SLM whilst applying a spiral-phase filter to the spatially separate beam reaching the camera. Once again the integration of ghost imaging into a well established imaging technique provided a drastic reduction in the number of photons necessary to acquire such an image, expanding the repertoire of low-light applications of ghost imaging.

The low-light capabilities of our ghost imaging that were presented throughout this thesis proved to have eclectic applications, however when compared to traditional imaging techniques the proposed benefits remained obscured by historical claims concerning its resolution. With an object illuminated by one photon whilst its spatial information is recorded via another, the fundamental resolution is entwined with the length scale over which these entangled photons were produced, a length scale which can be sub-wavelength. In the final experiment of this thesis I sought to clarify the resolution limits of ghost imaging as well as provide a review of the various aspects which contribute to this resolution. Whilst it proved true that the fundamental limitation on the resolution in a ghost imaging system

arises from the strength of the correlations, in practice this limit is unachievable. As is the case in a traditional imaging system the spatial coherence of the illumination, the resolution of the spatially resolving detector and the point spread function of the intervening optics all contribute to the final resolution of the acquired images. So although the length of the correlations can be sub-wavelength in the plane of the crystal, the accessible resolution was shown to be somewhat broadened by the other factions mentioned above.

The work presented in this thesis has extensively expanded the ghost imaging repertoire and represents the groundwork for future experiments involving the technique. Each experiment presented has the potential to be implemented in different imaging applications wherever a reduction in exposure is desired as well as situations where structural information of objects entirely opaque or translucent in the visible spectrum is sought. We hope the work here has dispelled some of the misconceptions of ghost imaging and will provide a useful resource for others performing ghost imaging experiments.

# Bibliography

[1] G. Sines and Y. A. Sakellarakis, "Lenses in antiquity," *Am. J. Archaeol.*, vol. 91, no. 2, pp. 191–196, 1987.

[2] M. Gatton, *Acts of Seeing*, ch. First Light: Inside the Palaeolithic camera obscura, pp. 146–153. Artakt and Zidane Press, 2009.

[3] P. A. Morris, R. A. Aspden, J. E. C. Bell, R. W. Boyd, and M. J. Padgett, "Imaging with a small number of photons," *Nat. Commun*, vol. 6, p. 5913, 2015.

[4] O. S. Magaña-Loaiza, G. A. Howland, M. Malik, J. C. Howell, and R. W. Boyd, "Compressive object tracking using entangled photons," *Appl. Phys. Lett.*, vol. 102, no. 23, p. 231104, 2013.

[5] L. A. Rozema, J. D. Bateman, D. H. Mahler, R. Okamoto, A. Feizpour, A. Hayat, and A. M. Steinberg, "Scalable spatial superresolution using entangled photons," *Phys. Rev. Lett.*, vol. 112, p. 223602, Jun 2014.

[6] J. H. Shapiro and R. W. Boyd, "The physics of ghost imaging," *Quantum Inf. Process.*, vol. 11, no. 4, pp. 949–993, 2012.

[7] G. Gariepy, N. Krstajic, R. Henderson, C. Li, R. R. Thomson, G. S. Buller, B. Heshmat, R. Raskar, J. Leach, and D. Faccio, "Single-photon sensitive light-in-flight imaging," *Nat. Commun.*, vol. 6, no. 6021, 2015.

[8] P. Llull, X. Liao, X. Yuan, J. Yang, D. Kittle, L. Carin, G. Sapiro, and D. J. Brady, "Coded aperture compressive temporal imaging," *Opt. Express*, vol. 21, pp. 10526–10545, May 2013.

[9] R. S. Aspden, D. S. Tasca, R. W. Boyd, and M. J. Padgett, "EPR-based ghost imaging using a single-photon-sensitive camera," *New J. Phys.*, vol. 15, no. 7, p. 073032, 2013.

[10] T. B. Pittman, Y. H. Shih, D. V. Strekalov, and A. V. Sergienko, "Optical imaging by means of two-photon quantum entanglement," *Phys. Rev. A*, vol. 52, pp. R3429–R3432, Nov 1995.

[11] A. Gatti, E. Brambilla, M. Bache, and L. A. Lugiato, "Ghost imaging with thermal light: comparing entanglement and classical correlation," *Phys. Rev. Lett.*, vol. 93, p. 093602, Aug 2004.

[12] R. S. Bennink, S. J. Bentley, R. W. Boyd, and J. C. Howell, "Quantum and classical coincidence imaging," *Phys. Rev. Lett.*, vol. 92, p. 033601, Jan 2004.

[13] R. S. Bennink, S. J. Bentley, and R. W. Boyd, "Two-photon coincidence imaging with a classical source," *Phys. Rev. Lett.*, vol. 89, p. 113601, Sep 2002.

[14] A. Gatti, E. Brambilla, M. Bache, and L. A. Lugiato, "Correlated imaging, quantum and classical," *Physical Review A*, vol. 70, no. 1, p. 013802, 2004.

[15] A. Gatti, E. Brambilla, M. Bache, and L. A. Lugiato, "Ghost imaging with thermal light: comparing entanglement and classical correlation," *Phys. Rev. Lett.*, vol. 93, no. 9, p. 093602, 2004.

[16] A. Valencia, G. Scarcelli, M. D'Angelo, and Y. Shih, "Two-photon imaging with thermal light," *Phys. Rev. Lett.*, vol. 94, no. 6, p. 063601, 2005.

[17] F. Ferri, D. Magatti, A. Gatti, M. Bache, E. Brambilla, and L. A. Lugiato, "High-resolution ghost image and ghost diffraction experiments with thermal light," *Phys. Rev. Lett.*, vol. 94, no. 18, p. 183602, 2005.

[18] J. S. Bell, "Bertlmann's socks and the nature of reality," *Le Journal de Physique Colloques*, vol. 42, no. C2, pp. C2–41, 1981.

[19] S. M. Barnett, *Quantum Information*. Oxford University Press, 2009.

[20] A. Einstein, B. Podolsky, and N. Rosen, "Can quantum-mechanical description of physical reality be considered complete?," *Phys. Rev.*, vol. 47, pp. 0777–0780, May 1935.

[21] J. S. Bell, *Speakable and Unspeakable in Quantum Mechanics.* Cambridge University Press, 2nd ed., 2004.

[22] T. Yarnall, A. F. Abouraddy, B. E. A. Saleh, and M. C. Teich, "Experimental violation of Bell's inequality in spatial-parity space," *Phys. Rev. Lett.*, vol. 99, p. 170408, Oct 2007.

[23] J. Romero, J. Leach, B. Jack, S. M. Barnett, M. J. Padgett, and S. Franke-Arnold, "Violation of Leggett inequalities in orbital angular momentum subspaces," *New J. Phys.*, vol. 12, p. 123007, Dec. 2010.

[24] B. Jack, J. Leach, J. Romero, S. Franke-Arnold, M. Ritsch-Marte, S. M. Barnett, and M. J. Padgett, "Holographic ghost imaging and the violation of a Bell inequality," *Phys. Rev. Lett.*, vol. 103, p. 083602, Aug 2009.

[25] W. Rosenfeld, D. Burchardt, R. Garthoff, K. Redeker, N. Ortegel, M. Rau, and H. Weinfurter, "Event-ready bell test using entangled atoms simultaneously closing detection and locality loopholes," *Phys. Rev. Lett.*, vol. 119, no. 1, p. 010402, 2017.

[26] E. J. S. Fonseca, P. H. S. Ribeiro, S. Padua, and C. H. Monken, "Quantum interference by a nonlocal double slit," *Phys. Rev. A*, vol. 60, no. 2, pp. 1530–1533, 1999.

[27] X. Y. Zou, L. J. Wang, and L. Mandel, "Induced coherence and indistinguishability in optical interference," *Phys. Rev. Lett.*, vol. 67, pp. 318–321, July 1991.

[28] P. H. S. Ribeiro, S. Pádua, J. C. Machado da Silva, and G. A. Barbosa, "Controlling the degree of visibility of Young's fringes with photon coincidence measurements," *Phys. Rev. A*, vol. 49, pp. 4176–4179, May 1994.

[29] R. M. Gomes, A. Salles, F. Toscano, P. H. S. Ribeiro, and S. P. Walborn, "Observation of a nonlocal optical vortex," *Phys. Rev. Lett.*, vol. 103, no. 3, p. 033602, 2009.

[30] S. P. Walborn, C. H. Monken, S. Padua, and P. H. Souto Ribeiro, "Spatial correlations in parametric down-conversion," *Phys. Rep.*, vol. 495, pp. 87–139, Oct. 2010.

[31] D. C. Burnham and D. L. Weinberg, "Observation of simultaneity in parametric production of optical photon pairs," *Phys. Rev. Lett.*, vol. 25, no. 2, pp. 84–87, 1970.

[32] J. Schneeloch and J. C. Howell, "Introduction to the transverse spatial correlations in spontaneous parametric down-conversion through the biphoton birth zone," *J. Opt.*, vol. 18, no. 5, p. 053501, 2016.

[33] R. W. Boyd, *Nonlinear Optics*. Academic Press, 3rd ed., 2008.

[34] G. B. Lemos, V. Borish, G. D. Cole, S. Ramelow, R. Lapkiewicz, and A. Zeilinger, "Quantum imaging with undetected photons," *Nature*, vol. 512, no. 7515, p. 409, 2014.

[35] C. C. Kim and G. Kanner, "Infrared two-color ghost imaging using entangled beams," in *SPIE Optical Engineering and Applications*, pp. 781503–781503, International Society for Optics and Photonics, 2010.

[36] S. Karmakar and Y. Shih, "Two-color ghost imaging with enhanced angular resolving power," *Phys. Rev. A*, vol. 81, p. 033845, Mar 2010.

[37] A. Fedrizzi, T. Herbst, A. Poppe, T. Jennewein, and A. Zeilinger, "A wavelength-tunable fiber-coupled source of narrowband entangled photons," *Opt. Express*, vol. 15, pp. 15377–15386, Nov 2007.

[38] W. Wiechmann, S. Kubota, T. Fukui, and H. Masuda, "Refractive-index temperature derivatives of potassium titanyl phosphate," *Opt. Lett.*, vol. 18, no. 15, pp. 1208–1210, 1993.

[39] S. Emanueli and A. Arie, "Temperature-dependent dispersion equations for KTiOPO4 and KTiOAsO4," *Appl. Optics*, vol. 42, no. 33, pp. 6661–6665, 2003.

[40] C. H. Monken, P. H. S. Ribeiro, and S. Padua, "Transfer of angular spectrum and image formation in spontaneous parametric down-conversion," *Phys. Rev. A*, vol. 57, no. 4, pp. 3123–3126, 1998.

[41] D. S. Tasca, R. S. Aspden, P. A. Morris, G. Anderson, R. W. Boyd, and M. J. Padgett, "The influence of non-imaging detector design on heralded ghost-imaging and ghost-diffraction examined using a triggered ICCD camera," *Opt. Express*, vol. 21, pp. 30460–73, Dec 2013.

[42] M. P. Buchin, "Low-light imaging-iccd, emccd, and scmos compete in low-light imaging," *Laser Focus World*, vol. 47, no. 7, p. 51, 2011.

[43] L. Zhang, L. Neves, J. S. Lundeen, and I. A. Walmsley, "A characterization of the single-photon sensitivity of an electron multiplying charge-coupled device," *J. Phys. B-At. Mol. Opt.*, vol. 42, no. 11, p. 114011, 2009.

[44] D. N. Klyshko, *Photons and Nonlinear Optics.* Gordon and Breach Science Publishers, 1988.

[45] G. M. Morris, "Image correlation at low light levels: a computer simulation.," *Appl. optics*, vol. 23.18, no. 3152-3159., 1984.

[46] E. J. Candès, J. Romberg, and T. Tao, "Robust uncertainty principles: Exact signal reconstruction from highly incomplete frequency information," *IEEE T. Inform. Theory*, vol. 52, no. 2, pp. 489–509, 2006.

[47] J. Romberg, "Imaging via compressive sampling [introduction to compressive sampling and recovery via convex programming]," *IEEE Signal Proc. Mag.*, vol. 25, no. 2, pp. 14–20, 2008.

[48] D. L. Donoho, "Compressed sensing," *IEEE T. Inform. Theory*, vol. 52, no. 4, pp. 1289–1306, 2006.

[49] G. K. Wallace, "The jpeg still picture compression standard," *IEEE transactions on consumer electronics*, vol. 38, no. 1, pp. xviii–xxxiv, 1992.

[50] Y. Shechtman, Y. C. Eldar, A. Szameit, and M. Segev, "Sparsity based sub-wavelength imaging with partially incoherent light via quadratic compressed sensing," *Opt. Express*, vol. 19, pp. 14807–22, Aug 2011.

[51] K. R. Rao and P. Yip, *Discrete cosine transform: algorithms, advantages, applications.* Academic press, 2014.

[52] R. S. Aspden, N. R. Gemmell, P. A. Morris, D. S. Tasca, L. Mertens, M. G. Tanner, R. A. Kirkwood, A. Ruggeri, A. Tosi, R. W. Boyd, G. S. Buller, R. H. Hadfield, and M. J. Padgett, "Photon-sparse microscopy: visible light imaging using infrared illumination," *Optica*, vol. 2, no. 12, pp. 1049–1052, 2015.

[53] V. Studer, J. Bobin, M. Chahid, H. S. Mousavi, E. Candes, and M. Dahan, "Compressive fluorescence microscopy for biological and hyperspectral imaging," *Proceedings of the National Academy of Sciences*, vol. 109, no. 26, pp. E1679–E1687, 2012.

[54] N. Radwell, K. J. Mitchell, G. M. Gibson, M. P. Edgar, R. Bowman, and M. J. Padgett, "Single-pixel infrared and visible microscope," *Optica*, vol. 1, no. 5, pp. 285–289, 2014.

[55] R. W. Boyd and C. H. Townes, "An infrared upconverter for astronomical imaging," *Appl. Phys. Lett.*, vol. 31, no. 7, p. 440, 1977.

[56] J. S. Dam, C. Pederson, and P. Tidemand-Lichtenberg, "High-resolution two-dimensional image upconversion of incoherent light," *Opt. Lett.*, vol. 35, no. 22, pp. 3796–3798, 2010.

[57] K. Huang, X. Gu, H. Pan, E. Wu, and H. Zeng, "Few-photon-level two-dimensional infrared imaging by coincidence frequency upconversion," *Appl. Phys. Lett.*, vol. 100, no. 15, p. 151102, 2012.

[58] W. Tang, Rand . Wu, X. Li, H. Pan, E. Wu, and H. Zeng, "Two-dimensional infrared and mid-infrared imaging by single-photon frequency upconversion," *Journal of Modern Optics*, vol. 62, no. 14, pp. 1126–1131, 2015.

[59] A. Tosi, A. D. Frera, A. B. Shehata, and C. Scarcella, "Fully programmable single-photon detection module for ingaas/inp single-photon avalanche diodes with clean and sub-nanosecond gating transitions," *Rev. Sci. Instrum.*, vol. 83, p. 013104, Jan 2012.

[60] K. W. Chan, J. P. Torres, and J. H. Eberly, "Transverse entanglement migration in Hilbert space," *Phys. Rev. A*, vol. 75, p. 050101, May 2007.

[61] M. P. Edgar, D. S. Tasca, F. Izdebski, R. E. Warburton, J. Leach, M. Agnew, G. S. Buller, R. W. Boyd, and M. J. Padgett, "Imaging high-dimensional spatial entanglement with a camera," *Nat. Commun.*, vol. 3, p. 984, 2012.

[62] S. Wäldchen, J. Lehmann, T. Klein, S. Van De Linde, and M. Sauer, "Light-induced cell damage in live-cell super-resolution microscopy," *Scientific reports*, vol. 5, p. 15348, 2015.

[63] D. J. Stephens and V. J. Allan, "Light microscopy techniques for live cell imaging," *Science*, vol. 300, no. 5616, pp. 82–86, 2003.

[64] F. Zernike, "Phase contrast, a new method for the microscopic observation of transparent objects.," *Physica*, vol. 9, no. 7, pp. 686–698, 1942.

[65] R. A. Lewis, "Medical phase contrast x-ray imaging: current status and future prospects," *Physics in medicine & biology*, vol. 49, no. 16, p. 3573, 2004.

[66] S. Fürhapter, A. Jesacher, S. Bernet, and M. Ritsch-Marte, "Spiral phase contrast imaging in microscopy," *Opt. Express*, vol. 13, no. 3, pp. 689–694, 2005.

[67] A. Jesacher, S. Fürhapter, S. Bernet, and M. Ritsch-Marte, "Shadow effects in spiral phase contrast microscopy," *Phys. Rev. Lett.*, vol. 94, no. 23, p. 233902, 2005.

[68] M. W. Beijersbergen, R. P. C. Coerwinkel, M. Kristensen, and J. P. Woerdman, "Helical-wavefront laser beams produced with a spiral phaseplate," *Opt. Commun.*, vol. 112, no. 5, pp. 321–327, 1994.

[69] C. Maurer, A. Jesacher, S. Bernet, and M. Ritsch-Marte, "What spatial light modulators can do for optical microscopy," *Laser & Photonics Reviews*, vol. 5, no. 1, pp. 81–101, 2011.

[70] V. Y. Bazhenov, M. V. Vasnetsov, and M. S. Soskin, "Laser beams with screw dislocations in their wavefronts," *Jetp Lett*, vol. 52, no. 8, pp. 429–431, 1990.

[71] R. A. Aspden, P. A. Morris, H. Ruiqing, Q. Chen, and M. J. Padgett, "Heralded phase-contrast imaging using an orbital angular momentum phase-filter," *Journal of Optics*, vol. 18, no. 5, p. 055204, 2016.

[72] A. Gatti, M. Bache, D. Magatti, E. Brambilla, F. Ferri, and L. A. Lugiato, "Coherent imaging with pseudo-thermal incoherent light," *Journal of Modern Optics*, vol. 53, no. 5-6, pp. 739–760, 2006.

[73] P. A. Moreau, E. Toninelli, P. A. Morris, R. S. Aspden, T. Gregory, G. Spalding, R. W. Boyd, and M. J. Padgett, "Resolution limits of quantum ghost imaging," *Optics Express*, vol. 26, no. 6, pp. 7528–7536, 2018.

[74] K. R. Popper, "Quantum theory and the schism in physics.," *Hutchinson*, 1982.

[75] F. M. Miatto, D. Giovannini, J. Romero, S. Franke-Arnold, S. M. Barnett, and M. J. Padgett, "Bounds and optimisation of orbital angular momentum bandwidths within parametric down-conversion systems," *Eur. Phys. J. D*, vol. 66, no. 7, p. 178, 2012.

[76] R. S. Aspden, D. S. Tasca, A. Forbes, R. W. Boyd, and M. J. Padgett, "Experimental demonstration of Klyshko's advanced-wave picture using a coincidence-count based, camera-enabled imaging system," *J. Mod. Optic.*, vol. 61, no. 7, pp. 547–551, 2014.

[77] A. Sudbery, "Popper's variant of the epr experiment does not test the copenhagen interpretation," *Philosophy of Science*, vol. 52, no. 3, pp. 470–476, 1985.

[78] M. J. Collett, R. Loudon, and C. W. Gardiner, "Quantum theory of optical homodyne and heterodyne detection," *Journal of Modern Optics*, vol. 34, no. 6-7, pp. 881–902, 1987.

[79] Y.-H. Kim and Y. Shih, "Experimental realization of popper's experiment: Violation of the uncertainty principle?," *Foundations of Physics*, vol. 29, no. 12, pp. 1849–1861, 1999.

[80] E. Bolduc, E. Karimi, K. Piché, J. Leach, and R. W. Boyd, "Quantum imaging with undetected photons," *arXiv preprint arXiv:1401.4318*, 2014.

[81] J. Reintjes and M. Bashkansky, "Considerations on an optical test of popper's experiment," *Journal of Modern Optics*, vol. 63, no. 1, pp. 2–16, 2016.

[82] C. E. Shannon, "A mathematical theory of communication," *A.T. & T. Tech. J.*, vol. 27, no. 623, 1948.